IEEE Access
Multidisciplinary ⋮ Rapid Review ⋮ Open Access Journal

Received September 21, 2020, accepted October 8, 2020, date of publication October 12, 2020, date of current version October 22, 2020.

Digital Object Identifier 10.1109/ACCESS.2020.3030200

Adaptive Multichannel Terahertz Communication by Space-Time Shared Aperture Metasurfaces

HOOMAN BARATI SEDEH, (Student Member, IEEE), MOHAMMAD MAHDI SALARY, AND HOSSEIN MOSALLAEI, (Senior Member, IEEE)

Metamaterials Laboratory, Department of Electrical and Computer Engineering, Northeastern University, Boston, MA 02115, USA

Corresponding author: Hossein Mosallaei (hosseinm@ece.neu.edu)

This work was supported in part by the U.S. Air Force Office of Scientific Research (AFOSR) under Grant FA9550-18-1-0354.

ABSTRACT We propose a technique for adaptive multichannel communication in the low-terahertz frequency regime through simultaneous and independent multifrequency multibeam scanning via a single time-modulated metasurface consisting of graphene micro-patch antennas whose Fermi energy levels are modulated by radio-frequency biasing signals. For this purpose, we divide the metasurface aperture into interleaved orthogonally modulated sub-array antennas with distinct modulation frequencies, rendering a shared aperture in space-time. The higher-order frequency harmonics generated by the sub-arrays in such a space-time shared-aperture metasurface are mutually orthogonal as they do not yield an observable interference pattern. A distinct constant progressive modulation phase delay can be adopted in each sub-array to independently scan its corresponding higher-order frequency harmonics via dispersionless modulation-induced phase gradient with minimal sidelobe level and full angle-of-view over a wide bandwidth. The number of sub-arrays and distinct channels can be scaled easily without suffering from cross-talk due to orthogonality of the channels. The concept is established theoretically and verified through numerical simulations. We characterize active beam-scanning performance of the space-time shared aperture metasurface in terms of gain and half power beamwidth and their dependence to the array architecture. We consider both one-dimensional and two-dimensional interleaving for scanning the beams along elevation and azimuth angles. We also obtain the upper bounds for the number of independent channels attainable without compromising angle-of-view as 8 and 64 for one-dimensional and two-dimensional interleaving, respectively within the same physical aperture. Our results point toward high-capacity platforms with low size, weight and power for next generations of terahertz communication systems.

INDEX TERMS Time-modulated metasurface, shared-aperture antennas, beam steering, terahertz communication.

I. INTRODUCTION

The unprecedented growth of the data exchanged between wireless devices and the rapid emergence of high quality wireless services have raised the demand for the communication bandwidth and data transmission rates. This has motivated the migration of wireless networks toward utilization of carrier waves with higher frequencies beyond millimeter wave band for data collection and transmission which can offer larger bandwidth and higher speeds. Terahertz (THz) band (ranging from 0.1 THz to 10 THz) which has been untapped so far for communication purposes is envisioned as one of the enabling technologies for future generations of wireless communication mobile networks (such as 6G) to address the needs of high-speed and bandwidth-intensive applications. THz communications are expected to enable backhaul interconnection between existing networks as well as providing broadband services to several wireless devices in a distributed local network [1], [2]. The latter is of particular importance in wireless internet of things applications [3] where there is a need for new communication paradigms capable of simultaneously addressing multiple mobiles users in real-time with potentially independent services. The recent migration from internet of things (IoT) to internet of nano-things (IoNT) [4] also imposes certain constraints in terms of size, weight and power (SWaP) on

The associate editor coordinating the review of this manuscript and approving it for publication was Wei Liu.

the communication systems, calling for development of smart antennas with adaptive and tunable response capable of establishing multiple active data links through multibeam scanning in a multiple-input, multiple-output (MIMO) network while meeting the demands on the capacity and SWaP.

Several different techniques have been adopted previously for development of multibeam patterns across different frequency spectra including utilization of phased array antennas [5]–[7], graded metamaterials based on transformation optics [8]–[10], zero refractive index metamaterials [11], [12], lenses [13]–[16], and metasurfaces [17]–[25]. Among these approaches, metasurfaces consisting of a planar two-dimensional ensemble of subwavelength unit cells are of particular interest for on-chip devices and applications where the size and weight are highly constrained due to their small form factor and fabrication feasibility. Metasurfaces have enabled an precedent control over the wavefront of light beams through imparting abrupt geometric or resonant phase discontinuities to an incoming wave [26], [27]. In particular, they can steer the reflected or transmitted light to an arbitrary anomalous angle (as opposed to the specular angle) determined by the phase gradient through generalized Snell's laws. Therefore, they can function as reflect- and/or transmit-array antennas and are promising candidates for free-space optical communications. For increasing the capacity of metasurface antennas toward multiple access communication, the optical response of their constituent elements can be encoded in different channels across different dimensions such as polarization [17], frequency [22], and incident angle [21]. Nevertheless, typically the response of a single unit cell is highly correlated across these dimensions. In order to achieve controllable and independent functionalities in each channel, the shared-aperture concept has been borrowed from the field of array antennas [28]–[31] and has been employed in the realm of metasurfaces. Shared-aperture metasurfaces consist of interleaved or stacked sub-arrays of distinct unit cells each of which are designed to respond to a distinct incident frequency, polarization, or angle [21], [22], [32]–[36]. They can increase functionality of metasurfaces while reducing size and weight by decreasing the number of metasurface antenna units as well as bringing down the costs associated with fabrication. A special attention should be paid into eliminating the cross-talk between the distinct channels by minimizing the coupling between their corresponding unit cells in the design of a shared aperture metasurface to enable simultaneous and independent operation. The constituent unit cells of shared aperture metasurfaces so far have relied on resonant phase accumulation, geometric Pancharatnam-Berry (PB) phase shift, or a hybrid of both phase tuning mechanisms to realize the desired functionalities in separate channels. Employing geometric PB phase shift in a shared aperture metasurface with interleaved architecture allows for higher scalability in the number of channels due to its dispersionless property which guarantees the full phase coverage at each channel simply by rotating the elements in the sub-array corresponding to that channel around their optical axis without being affected by the coupling to the unit cells corresponding to other channels [32]–[34]. This is while the design of shared aperture metasurfaces relying on resonant phase shifts [36] and/or a stacked sub-array architecture [21], [22], [35] becomes more cumbersome due to nontrivial coupling effects leading to cross-talk which typically limits the number of attainable distinct channels.

Despite the multiplexed functionality of shared aperture metasurfaces and their great potential for enhanced capacity in free-space optical communication systems, a grand challenge facing these platforms is that their response is set in stone after they have been designed and cannot be changed afterward. As such, they cannot be used for adaptive communications by establishing active data links between mobile users in a network. An immense effort has been made recently to overcome this limitation of passive metasurfaces by exploiting mechanical, thermal and electrical tuning mechanisms such that the phase of scattered light from the metasurface can be controlled in real-time by control over external stimuli (such as strain, temperature or voltage) rather than the change in the geometry [37]–[40]. Among the proposed tuning mechanisms, electro-optical tuning approaches relying on free-carrier effects in semiconductors [41]–[43] and two-dimensional materials such as graphene [44]–[46] are of particular interest due to high speed, low power consumption, and robust continuous tunability of individual unit cells via an electrical biasing network. Such geometrically-fixed active metasurfaces enable electrical steering of the reflected or transmitted light toward a desired direction by adjusting the voltage-dependent phase of their constituent elements. Despite the expeditious growth in this area, these quasi-static tunable metasurfaces have certain drawbacks stemming from the limitations in the active materials and the underlying physical mechanisms giving rise to the phase tunability. In particular, most electro-optical metasurfaces exploit spectral shift and transition of a resonant mode supported by their constituent unit cells between over-coupled and under-coupled states to attain a wide phase modulation in response to the change in the voltage and optical properties of the active material [42]. This approach severely limits the dynamic phase modulation bandwidth which is inversely proportional to the quality factor of the resonance. Given that a high-Q resonant mode is required to yield an enhanced light-matter interaction with the low-dimensional active regions of the materials, dynamic phase modulation can only be obtained in a narrow bandwidth. The dynamic phase span is also limited by the tuning range and volume of the active region and is typically less than 2π which limits the angle-of-view (AoV) in beam-scanning performance. Moreover, due to strong correlation between the phase and amplitude in the resonant scattering regime, wide phase modulation comes at the cost of dramatic variations in amplitude giving rise to considerable spurious scattering and sidelobe levels (SLLs). In addition to these shortcomings, quasi-static active metasurfaces cannot meet the high demands on the capacity of the communication as their performance in a

shared-aperture metasurface will be limited to a few distinct channels due to reliance on resonant phase modulation which limits the scalability of such platforms in terms of number of independent channels in the account of nontrivial coupling effects between the resonant unit cells [47].

More recently, time-modulated metasurfaces (TMMs) have emerged as a new class of active metasurfaces in which the external stimuli controlling the optical properties of the metasurface are varying periodically in time [40], [48]–[50]. These metasurfaces have been shown to enable a wide range of novel physical phenomena including nonreciprocity [51]–[59], wavefront engineering [60]–[64], spatiotemporal light manipulation [65]–[67], signal amplification [68], [69], extreme energy accumulation [70], wideband impedance matching [71], pulse shaping and reversal [72]–[74], and camouflaging [75], [76]. A fundamental property of such metasurfaces is the frequency mixing functionality which leads to generation of higher-order frequency harmonics. It has been recently established that the wavefront of higher-order frequency harmonics generated by a TMM can be tuned via a dispersionless modulation-induced phase shift which can be controlled linearly by the modulation phase delay and closely resembles the geometric PB phase shift [60]. In particular, introducing a modulation phase delay of α to the modulation waveform of a TMM, the n-th frequency harmonic acquires a dispersionless phase shift of $n\alpha$ while maintaining a constant amplitude. This phase modulation mechanism elevates time-modulated active metasurfaces beyond their quasi-static counterparts as it can increase the dynamic phase modulation bandwidth while providing access to full phase span 2π with a uniform amplitude thus enabling full AoV and suppressing SLLs [60], [63]. Moreover, due to their frequency mixing property TMMs are inherently suited for establishing several active data links which can be simultaneously scanned via dispersionless modulation-induced phase shift thus enhancing the communication capacity by providing multiple access through frequency division and space division [63], [64]. Nevertheless, due to linear proportionality of the modulation-induced phase shift to the frequency harmonic order, the active links established at higher-order frequency harmonics cannot be controlled independently. In this work, we aim at tackling this challenge by bridging the concepts of shared aperture and time-modulated metasurfaces.

We introduce the concept of space-time shared aperture metasurfaces (STSAMs) to enable multifrequency multibeam scanning with simultaneous and independent control toward adaptive multichannel communication in the THz regime. For this purpose, we consider a geometrically-fixed dynamic metasurface consisting of graphene micro-patch antennas which is divided into several interleaved sub-arrays as shown in Figure 1. By applying engineered radio-frequency (RF) biasing signals with distinct frequencies to the constituent graphene unit cells of sub-array antennas, their Fermi energy levels are modulated in time giving rise to non-interfering mutually orthogonal higher-order frequency harmonics. Employing a progressive modulation phase delay in each sub-array allows for independent scanning of its higher-order frequency component without being affected by other sub-arrays due to the dispersionless property of modulation-induced phase shift and orthogonality of the frequency channels. As such, the proposed approach is quite flexible for creating an arbitrarily large number of distinct communication channels. We establish the concept theoretically followed by numerical simulations to verify the predictions using the graphene-based STSAM. The real-time beam scanning performance of the STSAM is characterized in terms of gain and and half power beamwidth and their dependence to the array architecture. We verify the simultaneous and independent beam scanning capability via both one-dimensional (1D) and two-dimensional (2D) interleaved STSAMs along elevation and azimuth angles. We also establish the upper bounds for the number of independent channels attainable through 1D- and 2D interleaved STSAMs consisting of sparse orthogonally modulated sub-arrays without compromising the AoV of the channels. The study shows the higher capacity of 2D-interleaved STSAMs compared to their 1D-interleaved counterparts for the same physical aperture size.

II. THEORETICAL FORMULATION

In this section, we will outline the theoretical formulation of a STSAM performance in beam steering by applying phased array antenna theory. As the starting point, we consider a reflective planar periodic two-dimensional array lying in the transverse $x-y$ plane consisting of subwavelength unit cells varying periodically in time, under the illumination of a normally incident plane wave at the operating frequency of f_0. Under the assumption that the modulation frequency is much smaller than the incident frequency ($f_m \ll f_0$), the incident and the steady-state reflected fields can be expressed as the following in time-domain

$$\begin{aligned} E_i(t) &= E_0 \exp(i\omega_0 t) \\ E_r(t) &= r(t) \cdot E_i(t) \end{aligned} \tag{1}$$

wherein E_0 is the amplitude of the incident wave, $\omega_0 = 2\pi f_0$ is the optical angular frequency and $r(t)$ is the time-varying reflection coefficient. When the constituent unit cells of the periodic array are periodically varying in time with a modulation frequency of f_m, the reflection coefficient can be expanded in form of a discrete Fourier series as $r(t) = \sum_n r_n \cdot \exp(in\omega_m t)$, in which $\omega_m = 2\pi f_m$ is the modulation angular frequency and r_n's are the Fourier series coefficients. This indicates the frequency mixing property of a TMM which yields a frequency spectrum of $f_n = f_0 + nf_m$ in the scattered fields with $n \in \mathbb{Z}$ being an integer denoting the frequency harmonic order. In the adiabatic regime of modulation where $f_m/f_0 \ll 1$, a one-to-one mapping can be made between the steady-state time-domain reflection coefficient at each instant of time to the quasi-static stationary reflection coefficient according to the bias at that time instant which is

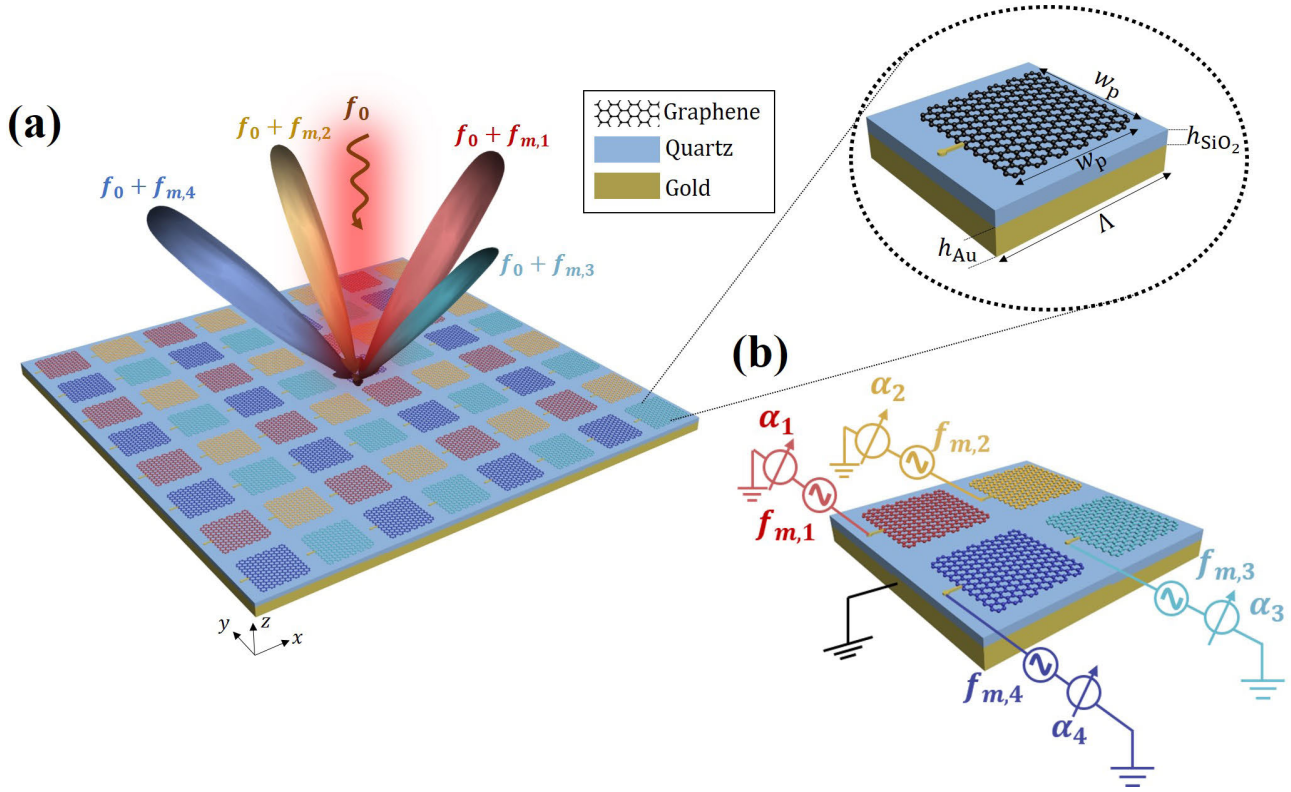

FIGURE 1. (a) Schematic depiction of the space-time shared aperture metasurface and its constituent elements illuminated by a normally incident TE-polarized wave. The STSAM consists of orthogonally modulated interleaved sub-arrays of graphene micro-patch antennas on top of a quartz substrate backed by a gold mirror. Each color corresponds to a different sub-array antenna with a distinct modulation frequency. The array architecture corresponds to a 2D-interleaved STSAM giving rise to 4 active communication channels whose corresponding main lobes can be steered in real-time along both elevation and azimuth angles, simultaneously and independently. The geometrical parameters of the graphene micro-patch antennas are set as $w_p = 10\ \mu$m, $h_{SiO_2} = 30\ \mu$m, $h_{Au} = 1\ \mu$m and $\Lambda = 14\ \mu$m for operation at the incident frequency of $f_0 = 1.3$ THz. (b) A single super cell of the STSAM showing the biasing of each sub-array with an RF signal of different frequency while incorporating RF phase shifters for control over the modulation phase delay.

determined by the modulation waveform [61]. As a result, introducing a modulation phase delay of α (equivalent to a temporal delay of $t_d = \alpha/\omega_m$) to the modulation waveform yields $r_\alpha(t) = \sum_n r_n \exp(in(\omega_m t + \alpha))$ for the steady-state reflection coefficient in the time-domain. As such, it can be inferred that the n-th frequency harmonic generated by the TMM acquires a phase shift of $n\alpha$, while maintaining a constant amplitude. Unlike the resonant phase shift, this modulation-induced phase is dispersionless and independent of the incident frequency [60]. Therefore, it is convenient to rewrite the reflected field from a TMM modulated with a modulation phase delay of α with respect to an arbitrary time reference, as

$$E_r(t) = E_0 \sum_n r_n \exp\left(i\left((\omega_0 + n\omega_m)t + n\alpha\right)\right) \tag{2}$$

Now we consider a finite quasi-periodic array consisting of unit cells modulated with progressive modulation phase delays of $\Delta\alpha_x$ and $\Delta\alpha_y$ between the immediately neighbor elements along $\hat{x}$ and $\hat{y}$ directions, respectively. Under the assumption of local periodicity, the farfield reflected field from such an array at a fixed radial distance of r_0 can be expressed as a superposition of plane waves with spatially-variant local phase and amplitude at different frequency harmonics in the following form

$$\begin{aligned} E_r(\theta, \varphi, t) &= E_0 \sum_n r_n \exp\left(i(\omega_0 + n\omega_m)t\right) \\ &\times \sum_{l_x} \exp\left(il_x\left(k_n \Lambda_x \sin(\theta)\cos(\varphi) + n\Delta\alpha_x\right)\right) \\ &\times \sum_{l_y} \exp\left(il_y\left(k_n \Lambda_y \sin(\theta)\sin(\varphi) + n\Delta\alpha_y\right)\right) \end{aligned} \tag{3}$$

where θ and φ are the elevation and azimuth angles, respectively, $k_n = (\omega_0 + n\omega_m)/c$ is the wavenumber corresponding to the n-th frequency harmonic, and Λ_x and Λ_y are the spacing between adjacent unit cells along $\hat{x}$ and $\hat{y}$ directions, respectively. It is straightforward to rewrite Eq. (3) in a more compact form as

$$\begin{aligned} E_r(\theta, \varphi, t) &= E_0 \sum_n r_n \exp\left(i(\omega_0 + n\omega_m)t\right) \end{aligned}$$

$$\times\left[\frac{1}{N_x}\frac{\sin\left(\frac{N_x}{2}\left(k_n\Lambda_x\sin(\theta)\cos(\varphi)+n\Delta\alpha_x\right)\right)}{\sin\left(\frac{1}{2}\left(k_n\Lambda_x\sin(\theta)\cos(\varphi)+n\Delta\alpha_x\right)\right)}\right]$$
$$\times\left[\frac{1}{N_y}\frac{\sin\left(\frac{N_y}{2}\left(k_n\Lambda_y\sin(\theta)\sin(\varphi)+n\Delta\alpha_y\right)\right)}{\sin\left(\frac{1}{2}\left(k_n\Lambda_y\sin(\theta)\sin(\varphi)+n\Delta\alpha_y\right)\right)}\right] \quad (4)$$

wherein N_x and N_y are the numbers of consisting elements along $\hat{x}$ and $\hat{y}$ directions, respectively. It should be remarked that the obtained expression for the farfield pattern of such a planar time-modulated array antenna incorporating a progressive modulation phase delay is different from conventional phased array antennas in that it yields a superposition of higher-order frequency harmonics whose directions can be controlled by adjusting the progressive modulation phase delays via RF phase shifters in the biasing network. In other words, in contrary to the conventional quasi-static metasurfaces, which exploit dispersive resonant phase shift to steer the reflected wave toward the desired direction, in the time-modulated platforms a modulation-induced phase shift is utilized which is dispersionless. As a result of dispersionless nature of modulation-induced phase shift, the time-modulated metasurface can remain functional for beam-steering across a wide range of incident frequencies (unlike its quasi-static counterpart), albeit the beam-steering efficiency changes with the change in frequency due to dispersive amplitude of generated higher-order frequency harmonic. The angles of the main lobe at the n-th generated frequency harmonic in elevation and azimuthal planes can be obtained by solving the following set of equations corresponding to the maxima of the patterns at higher-order frequency harmonics given in Eq. (4)

$$\begin{aligned} k_n\Lambda_x\sin(\theta_n)\cos(\varphi_n)+n\Delta\alpha_x&=2m_1\pi,\ m_1=0,\pm1,\pm2,\cdots\\ k_n\Lambda_y\sin(\theta_n)\sin(\varphi_n)+n\Delta\alpha_y&=2m_2\pi,\ m_2=0,\pm1,\pm2,\cdots \end{aligned} \quad (5)$$

A similar result could be obtained from the generalized Snell's law based on conservation of momentum and observing the linear dependence of modulation-induced phase gradient to the frequency harmonic order (n) and modulation phase delay (α). In this context, the reflection angles θ_n and φ_n are referred to as anomalous reflection angles (as opposed to specular reflection angle) while m_1 and m_2 denote the anomalous diffraction orders [60]. It is clear from Eq. (5) that by judiciously tuning $\Delta\alpha_x$ and $\Delta\alpha_y$, the angle of main lobes at higher-order frequency can be steered toward a desired direction in real-time while covering the full AoV (2π steradian (Sr) for a reflectarray). Furthermore, the higher-order frequency harmonics can be scanned simultaneously making TMMs well-suited for multi-point communication paradigms via frequency-division multicasting unlike the optical links based on static and quasi-static metasurfaces which support monochromatic point-to-point communication schemes. Nevertheless, it can be inferred from Eq. (5) that the angle of main lobes at higher-order frequency harmonics are correlated which is attributed to the linear dependence of modulation-induced phase gradient to the frequency harmonic order. This correlation hinders independent active control over the links established at distinct frequency harmonics which consequently limits the functionality of a TMM antenna in a distributed network where the users should be addressed simultaneously with potentially independent services.

To overcome this issue, we will divide the TMM aperture into interleaved sub-arrays each of which is modulated via the modulation frequency of $f_{m,p}$ while incorporating progressive modulation phase delays of $\Delta\alpha_{x,p}$ and $\Delta\alpha_{y,p}$ along $\hat{x}$ and $\hat{y}$ directions, respectively (the subscript p denotes the index of the sub-array antenna). In other words, instead of utilizing a fixed modulation frequency of f_m and fixed progressive modulation phase delays of $\Delta\alpha_x$ and $\Delta\alpha_y$, we will apply orthogonal biasing signals with alternating modulation frequencies and progressive modulation phase delays across the metasurface aperture, rendering a shared aperture in space-time. The division of metasurface aperture into orthogonally modulated sub-arrays can be performed across one or two spatial dimensions in the transverse plane giving rise to 1D- or 2D- interleaved configuration. The reflected field from such a STSAM can be expressed as a superposition over the frequency harmonics generated by different sub-arrays

$$\begin{aligned} &E_r(\theta,\varphi,t)\\ &=E_0\sum_p\sum_n r_{n,p}\exp\left(i(\omega_0+n\omega_{m,p})t\right)\\ &\quad\times\left[\frac{1}{N_x}\frac{\sin\left(\frac{N_x}{2}\left(k_{n,p}\Lambda_{x,p}\sin(\theta)\cos(\varphi)+n\Delta\alpha_{x,p}\right)\right)}{\sin\left(\frac{1}{2}\left(k_{n,p}\Lambda_{x,p}\sin(\theta)\cos(\varphi)+n\Delta\alpha_{x,p}\right)\right)}\right]\\ &\quad\times\left[\frac{1}{N_y}\frac{\sin\left(\frac{N_y}{2}\left(k_{n,p}\Lambda_{y,p}\sin(\theta)\sin(\varphi)+n\Delta\alpha_{y,p}\right)\right)}{\sin\left(\frac{1}{2}\left(k_{n,p}\Lambda_{y,p}\sin(\theta)\sin(\varphi)+n\Delta\alpha_{y,p}\right)\right)}\right] \end{aligned} \quad (6)$$

wherein $\Lambda_{x,p}$ and $\Lambda_{y,p}$ are the spacing between adjacent unit cells of the p-th sub-array along $\hat{x}$ and $\hat{y}$ directions, respectively. It is clear from Eq. (6) that a unique set of modulation frequency and progressive modulation phase delay is assigned to each sub-array p leading to establishment of distinct radiation patterns at distinct frequencies which can be tuned independently by individual control over the progressive modulation phase delays of each sub-array via RF phase shifters. The angles of the main lobe at the n-th generated frequency harmonic corresponding to the p-th sub-array in elevation and azimuthal planes denoted by $\theta_{n,p}$ and $\varphi_{n,p}$, respectively can be found as

$$\begin{aligned} k_{n,p}\Lambda_{x,p}\sin(\theta_{n,p})\cos(\varphi_{n,p})+n\Delta\alpha_{x,p}&=2m_1\pi\\ k_{n,p}\Lambda_{y,p}\sin(\theta_{n,p})\sin(\varphi_{n,p})+n\Delta\alpha_{y,p}&=2m_2\pi \end{aligned} \quad (7)$$

This formulation illustrates the capability of STSAMs in adaptive multichannel communication by establishing active data links at distinct frequencies which can be scanned in

space simultaneously and independently. It should be mentioned that while the higher-order frequency harmonics of a specific order $n \neq 0$ generated by all sub-arrays are mutually orthogonal as long as the applied modulation frequency to the sub-arrays are different (i.e. for each two sub-arrays of p and q, $f_0 + nf_{m,p} \neq f_0 + nf_{m,q}$ when $f_{m,p} \neq f_{m,q}$), in order to ensure the mutual orthogonality of all frequency mixing products generated by the sub-arrays, the modulation frequency of each pair of sub-arrays should be non-integer irrational divisor of each other (i.e. for each two sub-arrays of p and q, $f_{m,p}/f_{m,q} \in \mathbb{Q}'$). This condition ensures that there is no spectral overlap between the output frequency spectrum of the sub-arrays except at the fundamental frequency harmonic ($n = 0$), thus removing the cross-talk between the independent communication channels by rendering the established links at higher-order frequency harmonics orthogonal in the sense that they do not yield an observable spatial interference pattern and can be separated via spectral filtering.

III. DESIGN OF GRAPHENE-BASED DYNAMIC METASURFACE

In order to demonstrate the applicability of STSAM concept for adaptive multichannel THz communication and to numerically verify the predictions of the formulation outlined in the previous section, we will design and model a reflective STSAM by utilizing graphene patch micro-antennas as its constituent unit cells. Graphene is one of the most well-known 2D materials whose surface conductivity can be tuned via field effect modulation of its Fermi energy level under application of an external bias voltage in a parallel capacitor configuration. A mono-layer graphene can be viewed as a one-atom thick semiconductor which can interact strongly with THz and mid-infrared light by supporting localized plasmons generated as a result of collective oscillation of free carriers [77], [78]. Due to its extreme thinness, electrical tunability, large-scale fabrication feasibility, and plasmonic response, graphene has been widely used for realization of gate-tunable dynamic metasurfaces [44]–[46]. Furthermore, the short response time of carriers in 2D materials enable modulation speeds up to several tens of GHz [79], making graphene an ideal candidate for realization of time-modulated devices by employing RF biasing signals for its modulation [58], [60].

The schematic of the proposed STSAM for dynamic operation in the low-THz frequency regime (around $f_0 = 1.3$ THz) is shown in Fig. 1 which consists of a 2D array of graphene patch micro-antennas mounted on top of a quartz (SiO_2) substrate backed by a gold mirror. The metasurface is illuminated by a normally incident transverse electric (TE) polarized plane wave (electric field is along x axis). Given that the feature sizes of a resonant metasurface in the low-THz regime is in order of several microns, the proposed configuration can be biased through a two-dimensional biasing grid in the plane of metasurface addressing each individual patch independently. Furthermore, vertical interconnect access (via) can be used to bias graphene patches through a feeding network lying on the plane below the metasurface [80], [81]. Each graphene patch antenna is considered to be modulated individually via an RF biasing signal whose phase delay can be controlled by incorporating RF phase shifters in the biasing network. In order to minimize the required voltage amplitudes to attain a certain level of Fermi energy level, ultrathin layers of a gate dielectric (e.g. alumina) and doped polycrystalline silicon can be be added between graphene patches and quartz substrate which will have negligible impact on the optical response while enhancing field effect modulation by applying bias voltages between the doped silicon layer and graphene patches [82], [83].

The permittivity of the quartz substrate is considered as $\epsilon_{SiO_2} = 3.75$ while the complex permittivity of gold is modeled by its Drude dispersion model. The complex surface conductivity of graphene can be accurately modeled based on the Kubo formula [84] as a summation over the interband and intraband transition contributions, i.e. $\sigma_g(\omega, E_f) = \sigma_{intra}(\omega, E_f) + \sigma_{inter}(\omega, E_f)$ with ω and E_f being incident angular frequency and Fermi energy level of graphene, respectively. In the frequency range of our interest here (i.e., 0.1–2 THz), the interband contribution can be neglected and thus the conductivity of the graphene can be written as [85]

$$\sigma_g(\omega, E_f) = \frac{2e^2}{\pi\hbar^2} \frac{k_B T}{\omega + i\tau^{-1}} \left(\frac{E_f}{2k_B T} \right) \tag{8}$$

where e is the electron charge and k_B is the Boltzmann constant, and $T = 300$ K is the temperature. In this paper, we have considered the relaxation time as $\tau = 0.5$ ps which can be achieved via state of the art of fabrication technology [86]–[89].

In order to achieve an optimal performance for the STSAM, we seek to achieve a pure frequency mixing by minimizing the undesired frequency mixing products and maximizing the frequency conversion of time-modulated metasurface to the first-order up-modulated frequency harmonic. Since the frequency conversion performance is determined by the temporal evolution of the quasi-static phase and amplitude [61], [66], we aim at maximizing the dynamic phase span of the metasurface by varying the Fermi energy level. Current research on graphene demonstrated that the Fermi energy level varies in a limited range when it is tuned with electrical biasing [45]. In particular, we limit ourselves to the Fermi energy level (E_f) within the range of 0 - 0.5 eV which has been shown to be attainable via gate biasing in recent experimental demonstrations [45]. The geometrical dimensions of the unit cell are set accordingly as $w_p = 10\ \mu$m, $h_{SiO_2} = 30\ \mu$m, $h_{Au} = 1\ \mu$m and $\Lambda = 14\ \mu$m, following a comprehensive parametric study. It should be mentioned that as the exploited unit cells are consisting of a plasmonic material, their periodicities and patch dimensions are much smaller than that of the operative wavelength. In other words, the plasmonic dimensions are forced to be smaller than other consisting parts, such as the thickness of the substrate layer. This will consequently lead the plasmonic-based unit cells to have compact footprints. However, the proposed unit cell

can be realized with the current state-of-the-art of fabrication technology as its minimum feature size is larger than the current minimum achievable precision via optical and e-beam lithography [90]. In the following subsections, we numerically study the quasi-static and time-modulated performance of the gate-tunable metasurface with a periodic configuration to discuss its operating principle.

A. QUASI-STATIC PERFORMANCE

In order to characterize the quasi-static response of the metasurface (tunable response in the absence of temporal modulation) by varying the Fermi energy level of graphene patches, we utilize an in-house built solver based on rigorous coupled wave analysis (RCWA) [91] capable of accurate modeling of graphene gratings as zero-thickness two-dimensional spatial patterns of surface conductivity [92]. The reflection amplitude and phase of the metasurface are calculated as functions of incident frequency for different Fermi energy levels of graphene patches and the results are shown in Fig. 2(a) and (b), respectively. The results indicate a resonant mode supported by the metasurface which can be identified by the dip in the reflection amplitude spectrum accompanied by a steep spectral phase accumulation. In order to characterize the resonance, the amplitudes of magnetic and electric fields within one unit cell of the metasurface in the $x-z$ plane are plotted in Fig. 2(c) for the normally incident plane wave polarized along x axis at the resonant frequency of $f = 1.138$ THz for $E_f = 0.15$ eV. As it can be seen, the electric field is strongly confined to the graphene patch while exhibiting an extreme enhancement around the edges. This nearfield profile is a manifestation of the localized surface plasmon resonance (LSPR) excited in the graphene patches. The strong localization of the field to graphene patches as a result of excited LSPR allows for effective tuning of the resonant response by varying graphene optical properties. Moreover, given that LSPR is a result of intrinsic resonant response of the individual unit cells rather than collective response of the elements, it enables a local manipulation of scattered fields by virtue of minimal long-range interactions.

As it can be observed from the results in Fig. 2(a) and (b), the LSPR frequency blueshifts toward larger frequencies by increasing the Fermi energy level. Furthermore, increasing the Fermi energy level leads to the increment in the internal loss of the resonant scattering channel which yields a transition of resonance from over-coupled to under-coupled state at Fermi energy levels between 0.2 eV and 0.25 eV. At the over-coupled state, the radiative loss is higher than the internal loss and the resonance yields a wide spectral phase accumulation with a span of almost 2π. This is while at the under-coupled state, the internal loss exceeds the radiative loss suppressing the spectral phase accumulation to a span of less than π. The reader is referred to [42] for more discussion on the interplay between the radiative and internal losses on the state of resonance (over-coupled and under-coupled) via coupled mode theory (CMT). The transition between over-coupled and under-coupled states is accompanied by a flip in the phase spectrum (i.e. change in the sign of group delay) which yields a wide phase swing at a single operating frequency by varying the Fermi energy level. Nevertheless, at the critical coupling state, the absorption is in its maxima which consequently leads to low efficiency. This approach has been previously used for dynamic phase modulation of THz and infrared lights in tunable metasurfaces based on graphene [44]–[46] and indium-tin-oxide [41]–[43]. We choose the operating frequency as $f_0 = 1.3$ THz as denoted by the dashed line in Fig. 2(a) and (b) to attain an optimal trade-off between the reflection amplitude efficiency and dynamic phase span. The reflection amplitude and phase at this frequency are shown as functions of Fermi energy level of graphene patch antennas in Fig. 2(d) and (e), respectively.

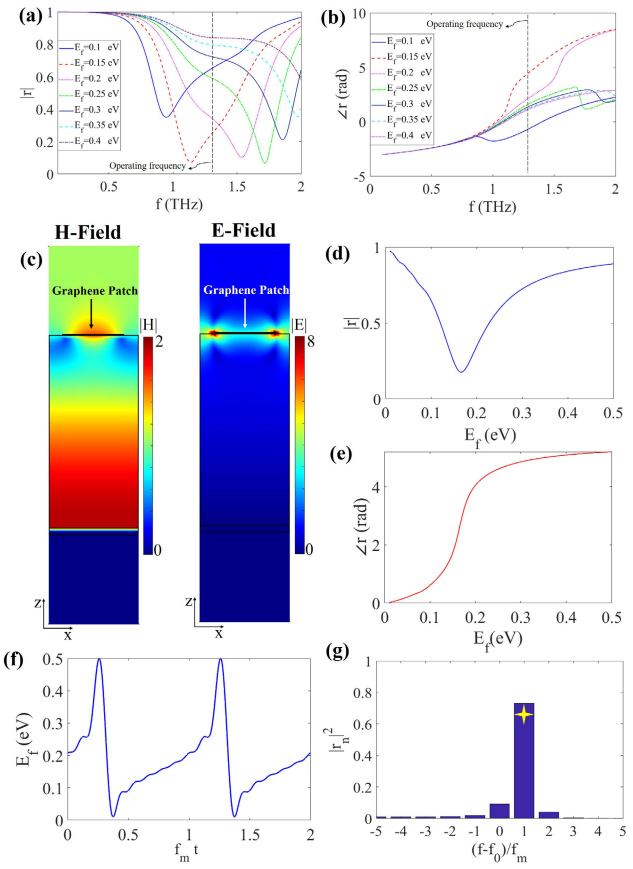

FIGURE 2. (a) The amplitude and (b) phase of the reflection coefficient from the metasurface calculated as functions of incident frequency for different Fermi energy levels of graphene patch antennas (E_f). The vertical dashed line marks the operating frequency of $f_0 = 1.3$ THz. (c) The calculated nearfield distribution of magnetic and electric fields within one unit cell of the metasurface in the x-z plane under normal incidence of an x-polarized plane wave at the resonant frequency of $f = 1.138$ THz for $E_f = 0.15$ eV. (d) The amplitude and (e) phase of the reflection calculated as functions of Fermi energy level ranging from 0.0 eV to 0.5 eV at the operating frequency of $f_0 = 1.3$ THz. (f) The optimized modulation waveform for the Fermi energy level to yield serrodyne frequency translation to the first-order up-modulated frequency harmonic. (g) The output frequency spectrum of the time-modulated metasurface showing the normalized frequency conversion efficiency vs the frequency harmonic orders, corresponding to the optimized modulation waveform in (f).

A dynamic phase span of $\approx 310°$ is achieved while the reflection amplitude varies between 0.2 and 1 across the phase modulation range. It should be remarked that in principle such dynamic phase modulation allows for steering of reflected light toward a desired direction by adjusting the applied bias voltage to the individual unit cells to imprint a linear phase gradient across the metasurface. Nevertheless, due to limited phase span (less than 2π) and dramatic variations of amplitude during phase modulation, such quasi-static tunable metasurface has a limited AoV and gives rise to considerable SLLs and spurious scattering. Furthermore, the bandwidth of dynamic phase modulation is limited due to limited bandwidth of resonant phase accumulation [41], [44]. These limitations and drawbacks can be alleviated by introducing time-modulation and exploiting the dispersionless modulation-induced phase shift of higher-order frequency harmonics which provides access to 2π phase span with uniform amplitude at all incident frequencies, albeit with different amplitude efficiencies [60], [63].

B. TIME-MODULATED PERFORMANCE

In order to calculate the output frequency spectrum of the dynamic metasurface whose Fermi energy level is modulated periodically in time with a given waveform, we construct the steady-state reflected field in time-domain via one-to-one mapping of the field at each instant of time to the quasi-static fields corresponding to the applied Fermi energy level at that time instant, and subsequently taking the Fourier transform of the steady-state time-domain field to arrive at the output frequency spectrum [61], [66]. This approach is valid in the adiabatic regime of modulation where the modulation frequency is much smaller than the excitation frequency ($f_m \ll f_0$). It is noteworthy that in this modulation regime, the modulation frequency does not lead to a noticeable change in the frequency conversion performance and it merely determines the spectral position of higher-order frequency harmonics ($f_n = f_0 + nf_m$). The frequency conversion performance of a TMM described by the spectral diversity and efficiency of the generated frequency harmonics is determined by the temporal evolution of the steady-state amplitude and phase which can be controlled by engineering the modulation waveform at any given incident frequency. It should be mentioned that in order to ideally realize an arbitrary output frequency spectrum, an independent control over the quasi-static phase and amplitude in time is required which is prohibitive in tunable metasurfaces due to correlation of phase and amplitude in the resonant scattering regime. While a phase-only temporal modulation can be adopted to arrive at a non-ideal output spectrum, utilizing an evolutionary algorithm for optimizing the modulation waveform can yield a more optimal response by taking into account the correlation and trade-offs between phase and amplitude. For this purpose, we have expressed the modulation waveform of the Fermi energy level in form of a truncated Fourier series as $E_f(t) = E_{f,0} + \sum_{n=1}^{n=8} A_n \sin(n\omega_m t) + B_n \cos(n\omega_m t)$, wherein $E_{f,0}$, A_n and B_n are the coefficients which are optimized by employing genetic algorithm (GA) to obtain the desired spectral diversity of frequency harmonics.

Here, we aim at maximizing the frequency conversion efficiency through pure frequency mixing; that is to convert the incident power at fundamental frequency to the first-order up-modulated frequency harmonic while minimizing the conversion to other frequency mixing products. For this purpose, the objective of the optimization to be maximized is defined as conversion efficiency to the first-order up-modulated frequency harmonic which is given by the reflected power residing at $f_0 + f_m$ over the total reflected power and can be expressed as $|r_{+1}|^2 / \sum_n |r_n|^2$ wherein $|r_n|$ denotes the reflection coefficient corresponding to the n-th frequency harmonic ($f_0 + nf_m$). The optimized Fermi energy modulation waveform and its corresponding normalized output frequency spectrum are shown in Fig. 2(f) and (g), respectively. The normalized frequency spectrum is obtained by calculating the frequency conversion efficiency to each harmonic order given by $|r_n|^2 / \sum_l |r_l|^2$. As it can be seen from the results, the optimized waveform exhibits a sawtooth-like pattern with broken time-reversal symmetry. This result well abides with the phase modulation prescription for serrodyne frequency translation which requires a sawtooth temporal phase profile modulating the quasi-static phase linearly over 2π span at each cycle of modulation [61], [66]. Moreover, it can be clearly seen from the normalized output spectrum that most of the reflected power is residing at the first up-modulated frequency harmonic ($n = +1$) yielding a normalized frequency conversion efficiency of $|r_{+1}|^2 / \sum_i |r_i|^2 = 74\%$. It should be remarked that the non-unity conversion efficiency is attributed to the limited quasi-static phase span and nonuniform quasi-static amplitude across the phase modulation range. In principle, a unity conversion efficiency can be obtained given that a tunable metasurface provides 2π phase with a uniform amplitude at the quasi-static operation. It should also be noted that despite the relatively high normalized frequency conversion efficiency, the overall frequency conversion efficiency is limited to 34% as the total reflected power is 46% of the incident power due to the dissipative loss of the graphene. In other words, 64% of the incident power is absorbed due to the dissipative loss of the graphene micro-patches ($P_{\text{loss}} = 0.64P_{\text{inc}}$), while 34% of the remaining part resides in the first harmonic ($P_{+1} = 0.34P_{\text{inc}}$) and the rest of the reflected power contains other harmonics ($P_{\text{n}} = 0.12P_{\text{inc}}$). These metrics characterize the efficiency of the antenna element. It is noteworthy to mention that with the expeditious growth in material science and rapid emergence of new 2-D materials with improved characteristics, higher efficiencies may be attainable in near future through advent of novel materials and/or design paradigms.

The frequency mixing property of TMMs as shown here make them highly suited for communications in turbulent conditions to avoid blockage of the communication links through adaptive tuning of the communication channel frequency.

IV. 1D-INTERLEAVED STSAM

In this section, we consider a 1D-interleaved STSAM by dividing the aperture of a finite metasurface consisting of 104×104 unit cells ($\approx 6.33\lambda_0 \times 6.33\lambda_0$ in size) along one spatial dimension (y-axis) into two sub-arrays each of which is modulated with an RF biasing signal with the optimized waveform shown in Fig. 2(e) having a different modulation frequency and incorporating different progressive modulation phase delays, toward establishing active data links with simultaneous and independent scanning capability. The metasurface is illuminated by a normally incident TE-polarized Gaussian beam with a waist of $r_0 = 3\lambda_0$ at the operating frequency of $f_0 = 1.3$ THz. The presented metasurface does not induce cross-polarization as the incident wave impinges normally on the metasurface and the exploited unit cells have equal dimensions and periodicity along x and y directions (i.e., $\Lambda_x = \Lambda_y = \Lambda$), which manifests a symmetry in their geometry.

It should be noted that a full-wave simulation of such a large-area time-modulated metasurface with multi-scale spatiotemporal characteristics is prohibitively expensive. As such, we employ the adiabatic analysis approach combined with field equivalence principle, based on the assumption of local periodicity. For this purpose, the locally scattered steady-state time-domain fields from the unit cells constructed by one-to-one mapping of the amplitude and phase at each time-instant to the quasi-static response obtained from full-wave RCWA simulations given the modulation waveform, modulation frequency and modulation phase delay are utilized for obtaining equivalent surface currents across the metasurface aperture at each instant of time via field equivalence principle. Once the steady-state time-domain surface currents are obtained, the scattered fields can be calculated everywhere in space at each instant of time by adopting proper dyadic Green's functions [63], [64], [66], [67]. The Fourier transform of the steady-state time-domain scattered fields are subsequently taken to arrive at the farfield reflection pattern at different frequency harmonics. In order to calculate the gain of STSAM antenna, first the intensities of the reflected fields generated by the sub-array antennas are obtained at different frequency harmonics as functions of elevation and azimuth angles. Then, the results are divided by the mean reflection intensity of an ideal antenna with the same aperture size which is excited with the same source. The gain of STSAM antenna at the n-th frequency harmonic generated by the p-th sub-array can be then expressed as $\text{Gain}_{n,p}(\theta, \varphi) = \frac{U(\theta,\varphi,f_0+nf_{m,p})}{\overline{U}}$ wherein $U(\theta, \varphi, f_0 + nf_{m,p})$ is the farfield intensity of the reflected field from the STSAM antenna at the frequency of $f_0 + nf_{m,p}$ and $\overline{U}$ is the mean reflection intensity of an ideal antenna given by $\overline{U} = P_{in}/4\pi$ with P_{in} being the input power [93].

A. ORTHOGONALITY CONDITION AND CROSS-TALK EFFECTS

In this subsection, we investigate the conditions for the orthogonality of the channels established by distinct sub-arrays in a 1D-interleaved STSAM and explore the cross-talk effects between them induced by the undesired frequency mixing products. As it was mentioned earlier in the manuscript, the frequency harmonics of a specific order $n \neq 0$ generated by interleaved sub-arrays of a STSAM are mutually orthogonal as long as their modulation frequencies are different. Nevertheless, in order to ensure the mutual orthogonality of all frequency mixing products generated by the sub-arrays, their output frequency spectra should not overlap except at the fundamental frequency which requires the modulation frequency of each pair of sub-arrays to be non-integer divisor of each other. Satisfaction of this orthogonality condition is essential to avoid interference between the pattern of sub-array p at the first up-modulated frequency harmonic of $f_0 + f_{m,p}$ which is the desired beam, and the pattern of other sub-arrays at the undesired frequency mixing products ($f_0 + nf_{m,q}$ for $n \neq +1$).

In order to corroborate this orthogonality condition, we study the farfield patterns of a STSAM consisting of two sub-arrays modulated with distinct modulation frequencies of $f_{m,1}$ and $f_{m,2}$, interleaved along the y-axis with a one-to-one ratio in the number of unit cells (i.e. the STSAM array architecture is $f_{m,1}; f_{m,2}; f_{m,1}; f_{m,2}, \ldots$). The spacing between the unit cells in the sub-arrays of this STSAM antenna will be $\Lambda_{y,1} = \Lambda_{y,2} = 2\Lambda$ and $\Lambda_{x,1} = \Lambda_{x,2} = \Lambda$. It should be remarked that as long as the modulation remains within the adiabatic regime (i.e. $f_{m,1} \ll f_0$ and $f_{m,2} \ll f_0$), the frequency conversion performance of the sub-arrays will be the same for the same modulation waveform yielding maximal conversion to the first-order up-modulated frequency harmonic, with the only difference being in the spectral position of the generated higher-order frequency harmonics.

First, we consider the case in which $f_{m,1} = f_0/256$ and $f_{m,2} = 2f_0/256$, i.e. the modulation frequency of the 1st sub-array is an integer divisor of that of the 2nd sub-array ($f_{m,2} = 2f_{m,1}$). The spatial distribution of modulation frequency across such STSAM is depicted in Fig. 3(a). The progressive modulation phase delays of the unit cells are set as $\Delta\alpha_{x,1} = 0$ and $\Delta\alpha_{y,1} = -k_0\Lambda_{y,1}\sin(15°)$ within sub-array 1, and $\Delta\alpha_{x,2} = 0$ and $\Delta\alpha_{y,2} = k_0\Lambda_{y,2}\sin(45°)$ within sub-array 2, in order to steer the dominant beams generated by the sub-arrays at their first-order up-modulated frequency harmonics toward angles given by $(\theta, \varphi)_{n,p} = (\theta, \varphi)_{+1,1} = (15°, 90°)$ and $(\theta, \varphi)_{n,p} = (\theta, \varphi)_{+1,2} = (45°, -90°)$, respectively by virtue of modulation-induced phase gradient according to Eq. (7). The distribution of modulation phase delay across the STSAM is shown in Fig. 3(b).

The farfield patterns of STSAM is calculated at the frequency channels established by the sub-arrays at their first-order up-modulated harmonic, namely channel 1 at $f_0 + f_{m,1}$ and channel 2 at $f_0 + f_{m,2}$ and the results are shown at the elevation plane ($|\varphi| = 90°$) in dB scale in Fig. 3(c). It should be noted that the angles denoted by $\theta < 0$ correspond to $(\theta, -90°)$ while the angles marked by $\theta > 0$ correspond to $(\theta, +90°)$. As it can be observed the main lobes at the channels established by the sub-arrays are steered toward the

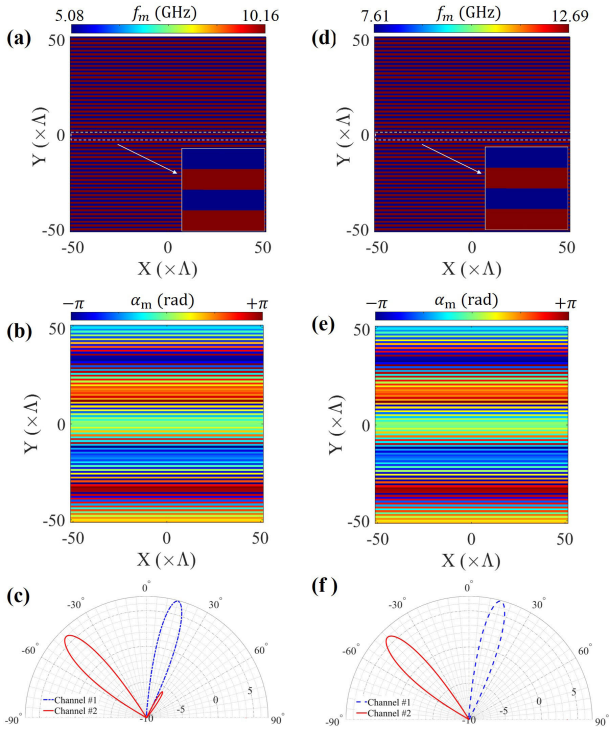

FIGURE 3. (a) The spatial distribution of modulation frequency across the 1-D interleaved STSAM in which the modulation frequency of the 1st sub-array is an integer divisor of that of the 2nd sub-array.(b) The modulation phase delay distribution across the 1D-interleaved sub-array set to steer the reflected beams at the first-order frequency harmonics of the sub-arrays toward elevation angles of $\theta_{+1,1} = 15°$ and $\theta_{+1,2} = -45°$ in the elevation plane. (c) The farfield pattern of the STSAM at the 1st and 2nd channels established by the 1st and 2nd sub-arrays, respectively in dB scale in the elevation plane ($|\varphi| = 90°$). (d)-(f) show the same as (a)-(c) for the 1D-interleaved STSAM in which the modulation frequencies of the sub-arrays are non-integer divisor of one another.

desired directions, abiding well with the theoretical predictions according to Eq. (7) and indicating the simultaneous and independent operation of the channels. While TMMs enable pattern synthesis with minimal spurious scattering due to sustaining the uniformity of amplitude during phase modulation via modulation-induced phase shift at higher-order frequency harmonics [63], a considerable sidelobe has appeared in the 2nd channel at $f_0 + f_{m,2}$. This is due to the fact that the modulation frequencies of the sub-arrays do not satisfy the non-integer divisibility condition which leads to cross-talk between the sub-arrays in the account of spectral overlap of the second-order up-modulated frequency harmonic generated by the 1st sub-array with the first-order up-modulated frequency harmonic established by the 2nd sub-array (i.e. $f_0 + 2f_{m,1} = f_0 + f_{m,2}$) giving rise to their spatial interference. Given that the modulation waveforms are optimized to minimize the undesired frequency mixing products (all harmonic orders except $n = +1$), the reflected power at the main lobe of the reflected beam at the second-order harmonic of the 1st sub-array is much smaller than that at the main lobe of the reflected beam at the first-order harmonic of the 2nd sub-array. Furthermore, due to linear proportionality of the modulation-induced phase gradient to the harmonic order, the second-order frequency harmonic generated by sub-array 1 is steered toward the angles of $(\theta, \varphi)_{n,p} = (\theta, \varphi)_{+2,1} \approx (30°, 90°)$. As such, this beam is manifested as a sidelobe at $\theta \approx 30°$ for the main lobe in the 2nd channel.

For elimination of the cross-talk between the sub-arrays and removing the generated sidelobe in the 2nd channel, the sub-arrays should be modulated orthogonally with non-integer divisible frequencies. In order to illustrate this, we consider the 1D-interleaved STSAM in which the modulation frequencies of the sub-arrays are changed to $f_{m,1} = 1.5f_0/256$ and $f_{m,2} = 2.5f_0/256$ with the progressive modulation phase delays remaining the same. The spatial distribution of modulation frequency and phase delay across the metasurface aperture in this case are demonstrated in Fig. 3(d) and (e), respectively. The farfield patterns in the 1st and 2nd channels corresponding to the first-order up-modulated frequency harmonic generated by the 1st and 2nd sub-arrays, respectively are obtained by calculating the STSAM antenna gain at $f_0 + f_{m,1}$ and $f_0 + f_{m,2}$, and the results are shown in Fig. 3(f). As it can be clearly observed, the sidelobe at the 2nd channel is suppressed completely and two directional beams with minimal SLL are obtained at two orthogonal channels which can be steered simultaneously and independently. It should be mentioned that although the chosen $f_{m,1}$ and $f_{m,2}$ are non-integer divisor of one another, the fifth-order frequency harmonic generated by the 1st sub-array overlaps with the third-order frequency harmonic generated by the 2nd sub-array due to the fact that $f_{m,1}/f_{m,2} = 3/5 \in \mathbb{Q}$ is a rational number. Nevertheless, since our goal is to engineer the patterns at the dominant first-order harmonics of the sub-arrays, such cross-talks do not have an impact on the multibeam scanning of the STSAM antenna and the non-integer divisibility is a sufficient condition to cancel out the cross-talk at the channels established by the sub-arrays. However, in order to avoid the spectral overlap of all frequency mixing products, the more general condition is for the modulation frequencies of sub-arrays to be a non-integer irrational divisor of one another ($f_{m,1}/f_{m,2} \in \mathbb{Q}'$). It should be noted that for an ideal lossless STSAM with unitary frequency conversion efficiency having the same aperture size, the peak gains corresponding to the main lobes in the 1st and 2nd channel are obtained as $G_{+1,1} = 18.9$ dB and $G_{+1,2} = 17.9$ dB, while they reduce to $G_{+1,1} = 7$ dB and $G_{+1,2} = 6$ dB for the presented case of Fig. 3 due to the non-unity frequency conversion efficiency and dissipative loss of the metasurface. It should be noted that for obtaining the corresponding gain of the proposed STSAMs, not only the efficiency of the elements but also the directivity and aperture efficiency were taken into account. In order to estimate, the effective aperture size, the well-known formula of $A_{\text{eff}} = \lambda^2 D/4\pi$ can be used. As the corresponding directivity of each sub-array is different from one another, each channel has a distinct aperture efficiency and effective aperture size. Moreover, changing the architecture of the sub-arrays also results in different aperture efficiency as a result of change

in the directivity and effective aperture size. It should also be mentioned that the aperture efficiency becomes lower as the deflection angle approaches to steeper values which is attributed to the decrease of its corresponding directivity due to increased impedance mismatch between the normally incident wave and oblique reflected wave. Finally, beam efficiency (BE), which indicates the amount of power in the main lobe compared to side lobes, is another important parameter that is expressed as [93]

$$\mathrm{BE}_p = \frac{\int_0^{2\pi}\int_0^{\theta_p} U(\theta,\varphi,f_0+nf_{m,p})\sin(\theta)d\theta d\varphi}{\int_0^{2\pi}\int_0^{\pi} U(\theta,\varphi,f_0+nf_{m,p})\sin(\theta)d\theta d\varphi} \tag{9}$$

which θ_p is the half-angle of the cone within which the percentage of the total power is to be found. By exploiting Eq. (9) for the proposed case of Fig. 3(f), the BE for first and second sub-arrays will be obtained as $\mathrm{BE}_1 = 97.82\%$ and $\mathrm{BE}_2 = 98.46\%$, respectively.

B. INDEPENDENT REAL-TIME BEAM-STEERING

In this subsection, we demonstrate the independent real-time beam steering at orthogonal channels established by the sub-arrays of STSAM antenna. According to Eq. (7), control over the progressive modulation phase delays in each sub-array of a STSAM allows for robust real-time tuning of the angle of the main lobes generated at its corresponding higher-order frequency harmonics without being affected by other sub-arrays. In order to rigorously verify this dynamic performance, we consider the 1D-interleaved STSAM with $f_{m,1} = 1.5f_0/256 = 7.61$ GHz and $f_{m,2} = 2.5f_0/256 = 12.69$ GHz. The progressive modulation phase delays corresponding to the 2nd sub-array are fixed as $\Delta\alpha_{x,2} = 0$ and $\Delta\alpha_{y,2} = -k_0\Lambda_{y,2}\sin(45°)$ yielding anomalous reflection angles of $(\theta,\varphi)_{+1,2} \approx (45°, 90°)$ at $f_0 + f_{m,2}$, while the progressive modulation phase delay corresponding to the 1st sub-array is fixed as $\Delta\alpha_{x,1} = 0$ along x-axis and is tuned along y-axis which can be done via RF phase shifters in the biasing network. Figure 4(a) and (b) show the gain of STSAM antenna in dB scale for the 1st and 2nd channels established by the 1st and 2nd sub-array at the frequencies of $f_0+f_{m,1}$ and $f_0+f_{m,2}$, respectively, as functions of progressive modulation phase delay of the 1st sub-array along y-axis ($\Delta\alpha_{y,1}$) and the observation angle in the elevation plane ($|\varphi| = 90°$). It is evident from the results that the angle of the main lobe in the 1st channel established by the 1st sub-array at $f_0 + f_{m,1}$ is steered from backward end-fire ($\theta = -90°$) to forward end-fire ($\theta = +90°$) with minimal SLL by varying its corresponding progressive modulation phase delay along y-axis ($\Delta\alpha_{y,1}$) from $-k_0\Lambda_{y,1}$ to $+k_0\Lambda_{y,1}$ following the anomalous reflection angle predicted by Eq. (7) (denoted by the dashed line) and yielding an AoV of 180°. Such all-angle scanning is afforded due to coverage of modulation-induced phase shift over the full phase span of 2π which is prohibitively challenging to attain in quasi-static tunable metasurfaces due to their limited resonant phase span [41], [44], [45]. On the other hand, the main lobe in the 2nd channel established by the 2nd sub-array at $f_0 + f_{m,2}$ remains fixed at $\theta = 45°$ and is not affected by the variations in $\Delta\alpha_{y,1}$. Similarly, tuning $\Delta\alpha_{y,2}$ enables real-time steering of the main lobe in the elevation plane in the 2nd channel without affecting the main lobe in the 1st channel. This clearly verifies the simultaneous and independent control over the distinct communication channels through multifrequency multibeam scanning with full AoV and low SLL.

As it can be observed from Fig. 4(a), the gain of STSAM antenna decreases as the beam is steered from broadside ($\theta = 0°$) toward end-fire angles ($|\theta| = 90°$) which is attributed to the decrement in the effective size of the aperture and increment in the impedance mismatch between the incident and reflected waves. The half power beamwidth (HPBW) of the reflected beam's main lobe in the 1st and 2nd channels are also calculated and shown in Fig. 4(c) and (d), respectively as functions of $\Delta\alpha_{y,1}$. While the HPBW of the main lobe in the 2nd channel is fixed and remains unaffected as expected, the HPBW of the main lobe in the 1st channel decreases as the beam is steered from the broadside toward end-fire angles yielding a decrement in directivity and gain. It should be noted that the gain in both channels are equal when the direction of their main lobes coincide at $\theta = 45°$ as the one-to-one ratio of the number of unit cells in the interleaved sub-arrays yields the same aperture size in both channels. Although, the gain of the STSAM antenna is limited by the frequency conversion efficiency and dissipative losses, it can

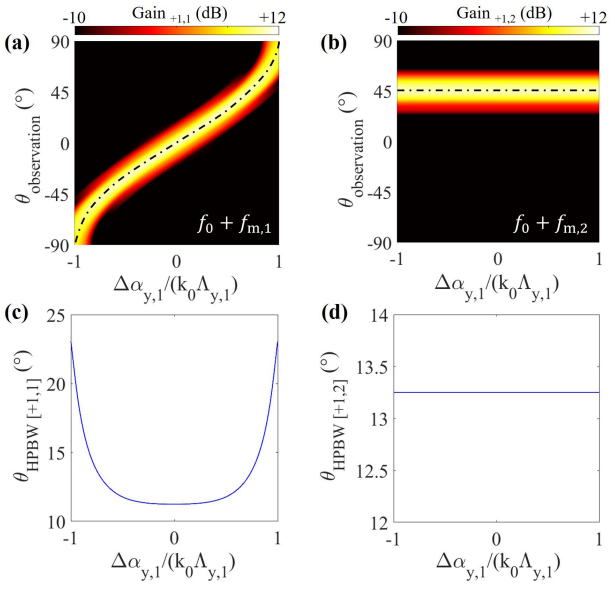

FIGURE 4. The gain of the 1-D interleaved STSAM antenna in dB scale for the (a) 1st channel and (b) 2nd channel corresponding to the first-order frequency harmonics generated by the 1st and 2nd sub-array, respectively as functions of farfield observation angle in the elevation plane ($|\varphi| = 90°$) and the progressive modulation phase delay along y-axis in the 1st sub-array, when $\Delta\alpha_{x,1} = \Delta\alpha_{x,2} = 0$ and $\Delta\alpha_{y,2} = -k_0\Lambda_{y,2}\sin(45°)$. The half power beamwidth of the main lobe in the (c) 1st channel and (d) 2nd channel corresponding to the first-order frequency harmonics generated by the 1st and 2nd sub-array, respectively as functions of the progressive modulation phase delay in the 1st sub-array.

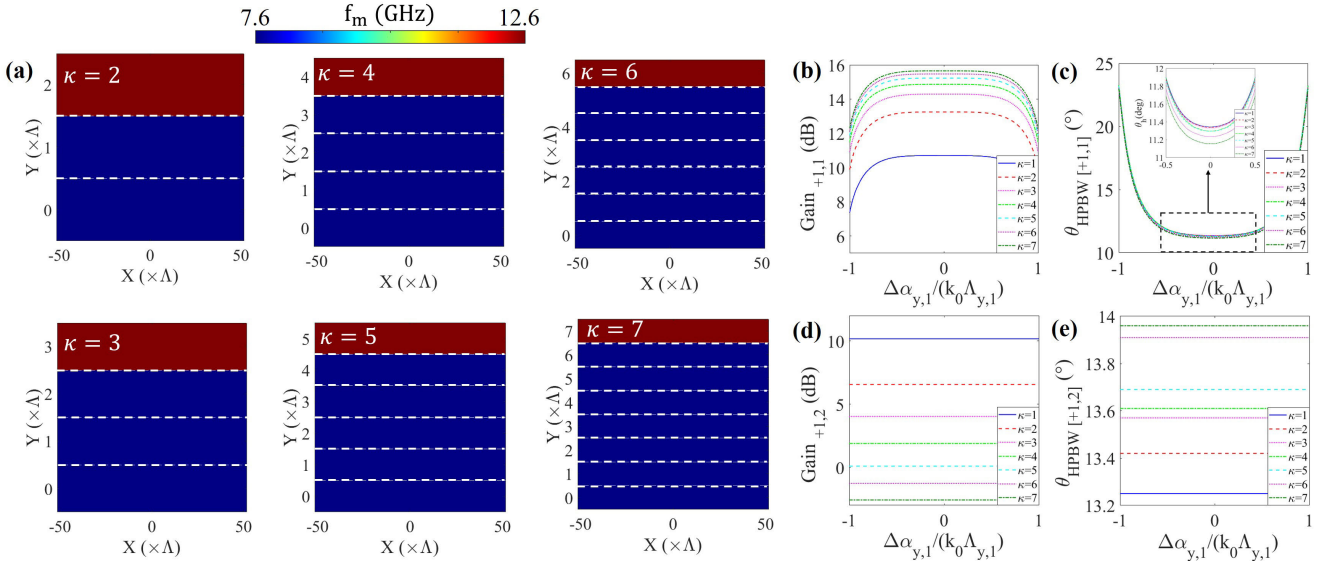

FIGURE 5. (a) The distribution of modulation frequency across one super cell of the 1D-interleaved STSAM for different array architectures with different ratios of the number of unit cells in the sub-arrays (κ). (b) The gain and (c) the half power beamwidth of the main lobe in the 1st channel established at the first-order up-modulated frequency harmonic generated by the 1st sub-array as functions of the progressive modulation phase delay along y-axis in the 1st sub-array. (d) and (e) show the same for the main lobe in the 2nd channel established at the first-order up-modulated frequency harmonic generated by the 2nd sub-array. In the results, we have fixed $\Delta\alpha_{x,1} = \Delta\alpha_{x,2} = 0$ and $\Delta\alpha_{y,2} = -k_0\Lambda_{y,2}\sin(45°)$.

be increased further by increasing the directivity (decreasing the HPBW) through enlarging the metasurface aperture. Here, the overall aperture size of the STSAM is chosen relatively small ($\approx 6.33\lambda_0 \times 6.33\lambda_0$) in order to accelerate the computation and facilitate comprehensive parametric studies.

C. EFFECTS OF ARRAY ARCHITECTURE ON REFLECTION CHARACTERISTICS

For the results presented in the previous subsections, the number of unit cells in the 1D-interleaved sub-arrays in the STSAM antenna were considered to have a one-to-one ratio yielding the same aperture size for both sub-arrays. Modifying the array architecture such that the number of unit cells in the 1st sub-array has a κ-to-one ratio with respect to that in the 2nd sub-array allows for redistributing the reflected power between the independent channels established by the sub-arrays and adjusting their power ratio levels by tuning the directivity of their corresponding main lobes due to the change in their aperture size.

In such an array architecture, the 2nd sub-array becomes sparser by increasing κ and the spacing between its constituent unit cells along y- axis scales by $\kappa + 1$ as $\Lambda_2 = (\kappa + 1)\Lambda$. It should be highlighted that as an array becomes sparser and its periodicity increases, its corresponding AoV for directional beam-steering may become limited due to emergence of secondary main lobes (also referred to as grating lobes) in the diffraction regime. The onset of the diffraction regime at the n-th frequency harmonic for the p-th sub-array under normal incidence can be characterized by the condition $1 \pm \sin(\theta_{n,p}) > \lambda_0/\Lambda_{y,p}$ according to the Floquet theory, wherein $\theta_{n,p}$ is the angle of the primary main lobe. This condition implies that when the spacing between the adjacent unit cells in a sub-array exceeds $\lambda_0/2$, i.e. $\Lambda_{y,p} > \lambda_0/2$ or $\lambda_0/\Lambda_p < 2$, the AoV becomes limited due to the onset of diffraction regime appearing at the end-fire angle, i.e. $1 + \sin(90°) > \lambda_0/\Lambda_p$. Obviously, the larger the spacing between the unit cells become, the more limited AoV gets due to the shift in the onset of diffraction regime toward smaller scanning angles. Considering that the operating wavelength is ≈ 16.48 times the spacing between the adjacent unit cells in the proposed metasurface ($\lambda_0 \approx 16.48\Lambda$), the maximum periodicity of the sparse sub-array can be 8Λ to ensure full AoV in the beam-scanning.

Here, we study the effect of array architecture on the reflection characteristics of the channels established by the 1D-interleaved sub-arrays. According to the above discussion, we limit our study to the cases where $\kappa \leq 7$ such that the generated beams by both sub-arrays at their corresponding first-order frequency harmonics can be scanned with full AoV. Figure 5(a) depicts the modulation frequency distribution across one super cell of the 1D-interleaved STSAM for different values of κ in which the modulation frequencies assigned to the 1st and 2nd sub-arrays are $f_{m,1} = 1.5f_0/256 = 7.61$ GHz and $f_{m,2} = 2.5f_0/256 = 12.69$ GHz, respectively. Similar to the previous sub-section, we fix the progressive modulation phase delays corresponding to the 2nd sub-array as $\Delta\alpha_{x,2} = 0$ and $\Delta\alpha_{y,2} = k_0\Lambda_{y,2}\sin(45°)$ yielding anomalous reflection angles of $(\theta, \varphi)_{+1,2} \approx (45°, 90°)$ at $f_0 + f_{m,2}$, while tuning the progressive modulation phase delay corresponding to the 1st sub-array along y-axis ($\Delta\alpha_{y,1}$) to steer the beam at $f_0 + f_{m,1}$ from backward to forward end-fire in the elevation plane when $\Delta\alpha_{x,1} = 0$. The gain and HPBW of the main lobe in the 1st channel established by the 1st sub-array at $f_0 + f_{m,1}$ are calculated as functions of $\Delta\alpha_{y,1}$ for different

values of κ and the results are shown in Fig. 5(b) and (c), respectively. Figure 5(d) and (e) show the same for the 2nd channel established by the 1st sub-array at $f_0 + f_{m,2}$. The gain and HPBW of the main lobe in the 1st channel decrease and increase, respectively as the beam is steered from broadside toward endfire by increasing $|\Delta\alpha_{y,1}|$, while those of the main lobe in the 2nd channel are independent from $\Delta\alpha_{y,1}$ as expected. On the other hand, increasing κ leads to increment in the gain and decrement in HPBW of the main lobe in the 1st channel while showing the reverse trend in the 2nd channel. This is due to the fact that increasing κ increases (decreases) the effective aperture size of the 1st (2nd) sub-array leading to increment (decrement) in the directivity of its corresponding main lobe and its share of the reflected power from STSAM. We note that the change in the HPBW of the main lobe in the 1st channel is significantly smaller compared to that of the main lobe in the 2nd channel which can be understood by observing that changing κ has a higher impact on the spacing between the unit cells of the 2nd sub-array ($\Lambda_2 = (\kappa + 1)\Lambda$), while the spacing between the constituent unit cells of the 1st sub-array along y axis ($\Lambda_{y,1}$) varies between Λ and 2Λ across the STSAM for all values of the κ.

The presented study in this subsection illustrates that the share of distributed power in the independent channels established by a STSAM antenna can be flexibly controlled by adjusting the array architecture and modifying the ratio of the number of unit cells in the sub-arrays, thus enabling realization of any asymmetric power distribution across the channels.

D. BEAM-STEERING IN TWO PLANES

The provided results for the STSAM performance so far have been corresponding to one-dimensional beam steering along the elevation angle (θ) in the elevation plane ($|\varphi| = 90°$). The 2D geometry of the constituent unit cells of the proposed dynamic metasurfaces allows for two-dimensional beam steering along both elevation and azimuth angles by employing a 2D biasing network which enables tuning of the modulation phase delay of the individual unit cells in each row and column. In order to examine such capability, we consider the STSAM consisting of 1D-interleaved sub-arrays with modulation frequencies of $f_{m,1} = 1.5f_0/256 = 7.61$ GHz and $f_{m,2} = 2.5f_0/256 = 12.69$ GHz along y-axis with a one-to-one ratio for the number of unit cells. Figure 6(a) demonstrates the distribution of modulation frequency across the STSAM aperture. Unlike the previous considered cases in the paper, the progressive modulation phase delays of the sub-arrays are modified along both x and y axes this time to steer the beams generated at their corresponding first-order frequency harmonics toward arbitrary elevation and azimuth angles. In particular, we set the progressive modulation phase delays as $\Delta\alpha_{x,1} = -k_0\Lambda_{x,1}\sin(30)\cos(110)$ and $\Delta\alpha_{y,1} = k_0\Lambda_{y,1}\sin(30)\sin(110)$ along x and y axis, respectively in the 1st sub-array, and as $\Delta\alpha_{x,2} = -k_0\Lambda_{x,2}\sin(50°)\cos(45°)$ and $\Delta\alpha_{y,2} = -k_0\Lambda_{y,2}\sin(50°)\sin(45°)$ along x and y axis, respectively in the 2nd sub-array.

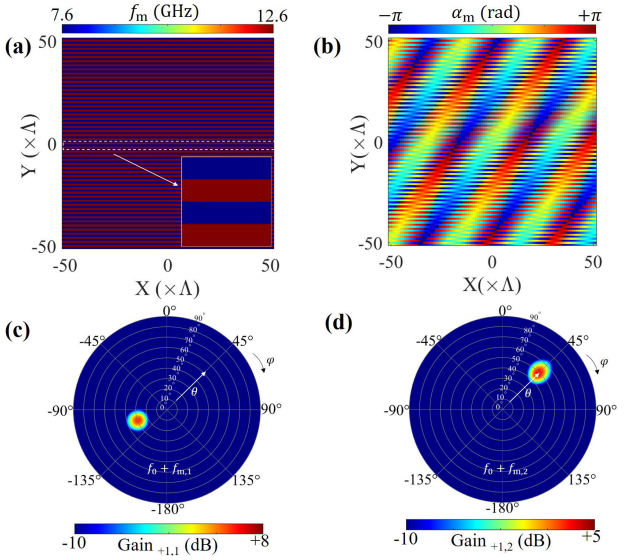

FIGURE 6. (a) The spatial distribution of modulation frequency across the 1D-interleaved STSAM. (b) The spatial distribution of modulation phase delay across the 1D-interleaved STSAM set in order to steer the beams at the first-order frequency harmonics generated by the sub-arrays along both azimuth and elevation angles toward $(\theta, \varphi)_{+1,1} = (30°, -110°)$ and $(\theta, \varphi)_{+1,2} = (50°, 45°)$. The 2D farfield pattern of the STSAM gain in (c) the 1st channel and (d) the 2nd channel established at the first-order frequency harmonics generated by the 1st and 2nd sub-array, respectively. The radial direction denotes the elevation angle while the polar angle marks the azimuth direction.

The resultant distribution of the modulation phase delay across the STSAM aperture is shown in Fig. 6(b). According to Eq. (7), this modulation phase delay distribution yields anomalous reflection angles of $(\theta, \varphi)_{+1,1} = (30°, -110°)$ and $(\theta, \varphi)_{+1,2} = (50°, 45°)$ in the 1st and 2nd channels corresponding to the first-order frequency harmonics of the beams generated by the 1st and 2nd sub-arrays, respectively. The 2D farfield patterns of the STSAM antenna gain in the 1st and 2nd channels corresponding to the frequencies of $f_0 + f_{m,1}$ and $f_0 + f_{m,2}$ are illustrated in Fig. 6(c) and (d), respectively wherein the radial direction denotes the elevation angle (θ) and the polar angle marks the azimuth angle (φ). Directive beams with $\mathrm{BE}_1 = 98.31\%$ and $\mathrm{BE}_2 = 97.74\%$ are generated with minimal SLL in both channels whose main lobe angles are in great agreement with the theoretical predictions based on Eq. (7). The gain of the main lobe in the 2nd channel is lower compared to that in the 1st channel despite the equal size of the sub-arrays which is due to fact that the generated beam in the 2nd channel is further from the broadside being in accordance with the results of study presented in Fig. 4.

The 2π phase coverage of modulation-induced phase gradient with uniform amplitude at higher-order frequency harmonics and the non-interfering patterns generated in the established channels by the orthogonally modulated sub-arrays enable simultaneous and independent multifrequency multibeam scanning with minimal SLL and full AoV which is 2π Sr for the STSAM reflectarray antenna.

V. 2D-INTERLEAVED STSAM

Hitherto, we have only studied 1D-interleaved STSAMs wherein the constituent sub-arrays modulated with distinct frequencies are interleaved along one spatial dimension (specifically along y-axis). The two-dimensional geometry of the unit cells in the proposed dynamic metasurface not only allows for two-dimensional beam steering through individual biasing of each unit cell but also enables 2D-interleaving by alternatingly varying the modulation frequency across the metasurface aperture along both transverse spatial dimensions (x and y). Such 2D-interleaved STSAM can dramatically increase the number of communication channels compared with a 1D-interleaved STSAM that has same physical area. In order to evaluate the beam scanning performance of a 2D interleaved STSAM, we divide the aperture of the finite metasurface consisting of 104×104 unit cells ($\approx 6.33\lambda_0 \times 6.33\lambda_0$ in size) into four sub-arrays interleaved along both x and y axes with the same number of unit cells. The spacing between the unit cells of each sub-array in such array architecture is $\Lambda_{x,1} = \Lambda_{x,2} = \Lambda_{x,3} = \Lambda_{x,4} = 2\Lambda$ and $\Lambda_{y,1} = \Lambda_{y,2} = \Lambda_{y,3} = \Lambda_{y,4} = 2\Lambda$. The sub-arrays are modulated with distinct frequencies of $f_{m,1} = 1.5f_0/256 = 7.61$ GHz, $f_{m,2} = 2.5f_0/256 = 12.69$ GHz, $f_{m,3} = 3.5f_0/256 = 17.77$ GHz, and $f_{m,4} = 5.5f_0/256 = 27.93$ GHz such that each pair of modulation frequencies are non-integer divisor of one another thus eliminating the cross-talk between the channels established at the first-order up-modulated frequency harmonics generated by the sub-arrays. The distribution of modulation frequency across the 2D-interleaved STSAM aperture is depicted in Fig. 7(a). The progressive modulation phase delays of the orthogonally modulated sub-arrays are set in accordance with Eq. (7) to yield anomalous reflection angles of $(\theta, \varphi)_{+1,1} = (50°, 22.5°)$, $(\theta, \varphi)_{+1,2} = (30°, 120°)$, $(\theta, \varphi)_{+1,3} = (40°, -60°)$, and $(\theta, \varphi)_{+1,4} = (20°, -160°)$, respectively. The resultant modulation phase delay across the 2D-interleaved STSAM aperture is shown in Fig. 7(b).

The 2D farfield patterns of the STSAM antenna gain in the four channels established by the 2D-interleaved sub-arrays are calculated and shown in Fig. 7(c)-(f), respectively. It can be seen from the results that a directive beam with minimal SLL and beam efficiency of $BE_1 = 97.23\%$, $BE_2 = 98.44\%$, $BE_3 = 97.69\%$, and $BE_4 = 98.96\%$ is generated in the four orthogonal channels which point toward the predefined anomalous reflection angles with high accuracy. The difference in the peak gains of the channels is attributed to the different distance of their main lobe from the broadside angle such that the further the main lobe angle is from the broadside direction, the lower gain it exhibits due to the decrement in the effective aperture size. It should also be noted that the peak gains in the four channels are smaller compared to those in the two channels established by a 1D-interleaved sub-array whose patterns are shown in Fig. 6(c) and (d) which is due to redirection of the incident power into more channels.

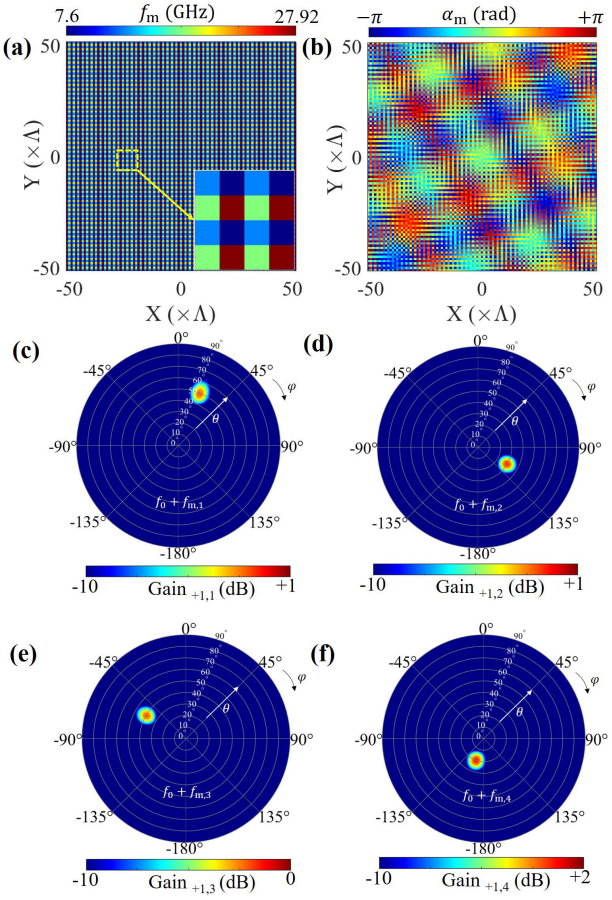

FIGURE 7. (a) The spatial distribution of modulation frequency across the 2D-interleaved STSAM. (b) The spatial distribution of modulation phase delay across the 2D-interleaved STSAM set in order to steer the beams at the first-order frequency harmonics generated by the sub-arrays along both azimuth and elevation angles toward $(\theta, \varphi)_{+1,1} = (50°, 22.5°)$, $(\theta, \varphi)_{+1,2} = (30°, 120°)$, $(\theta, \varphi)_{+1,3} = (40°, -60°)$, and $(\theta, \varphi)_{+1,4} = (20°, -160°)$. The 2D farfield pattern of the STSAM gain in (c) the 1st channel, (d) the 2nd channel, (e) the 3rd channel, and (f) the 4th channel established at the first-order frequency harmonics generated by the 1st, 2nd, 3rd, and 4th sub-array, respectively.

It can be inferred from these results that the 2D-interleaved STSAM yields simultaneous and independent multifrequency multibeam scanning with minimal SLL over full AoV, similar to its 1D-interleaved counterpart while allowing for integration of more channels within a metasurface platform with a fixed footprint. All the discussions on the effect of the array architecture on the reflection characteristics of the 1D-interleaved STSAMs brought in the previous section are also relevant for 2D-interleaved STSAMs in that the control over the ratio of the number of unit cells in different sub-arrays enables asymmetric redistribution of the reflected power across the orthogonal channels.

VI. SCALABILITY AND CAPACITY LIMIT

In principle, the number of integrated channels into 1D- and 2D-interleaved STSAMs can be chosen to be arbitrarily large and is only limited by the physical size of the aperture.

As long as the modulation frequencies of the sub-arrays comprising the STSAM are assigned such that the ones in each pair are non-integer divisor of one another, the patterns of the reflected fields at the first higher-order frequency harmonics generated by the sub-arrays can be controlled simultaneously and independently. Nevertheless, as the number of channels integrated into a fixed aperture increases, the HPBW of their corresponding main lobes increases due to decrement in the aperture size of the sub-arrays. Furthermore, the peak gain attainable for the main lobes corresponding to the frequency channels established by the orthogonally modulated sub-arrays decreases due to the decrement in the directivity (increment in the HPBW) of the beams as well as sharing the incident power between more number of channels. On the other hand, as the number of interleaved sub-arrays increases, each sub-array becomes sparser which can also limit its AoV in directive beam scanning due to appearance of secondary main lobes (grating lobes) at the onset of diffraction regime. This latter limitation poses an upper limit on the number of channels which can be integrated into an STSAM antenna without compromising the AoV for simultaneous and independent beam scanning in the established channels. Given that $\lambda_0 \approx 16.48\Lambda$ in the proposed metasurface design and bearing in mind that the condition for attaining full AoV at the first-order frequency harmonics generated by the p-th sub-array is $\Lambda_p \leq \lambda_0/2$, the maximum number of channels that can be integrated into the metasurface aperture without limiting the AoV is 8 for the 1D-interleaved STSAM and $8 \times 8 = 64$ for the 2D-interleaved STSAM.

In the following, we evaluate the beam-scanning performance of multichannel 1D-interleaved and 2D-interleaved STSAMs yielding maximum capacity without compromising AoV. For this purpose, the aperture of the finite metasurface consisting of 104×104 unit cells ($\approx 6.33\lambda_0 \times 6.33\lambda_0$ in size) is divided into $N = 8$ and $N = 64$ sub-arrays in the case of 1D-interleaved and 2D-interleaved STSAM, respectively. In each case, the modulation frequencies of the sub-arrays are chosen carefully such that the modulation frequencies of each pair of sub-arrays are non-integer divisor of each other to avoid cross-talk between the channels established at the first-order frequency harmonics. The distribution of modulation frequency across the metasurface aperture is shown in Fig. 8(a) and (b) for 1D-interleaved and 2D-interleaved STSAM, respectively. The progressive modulation phase delay of the sub-arrays is fixed as $\Delta\alpha_{x,p} = 0$ along the x-axis while it is set along y-axis in each sub-array to generate equally-spaced directional beams in the elevation plane ($|\varphi| = 90°$) within the angular range of $-60° < \theta < 60°$. For this purpose, the progressive modulation phase delay of p-th sub-array along y-axis is set as $\Delta\alpha_y = -k_0\Lambda_{p,y}\sin(-60° + \frac{120°}{N-1}(p-1))$ wherein $1 \leq p \leq N$ with $N = 8$ for the 1D-interleaved sub-array and $N = 64$ for the 2D interleaved sub-array. It should be noted that the choice of $-60° < \theta < 60°$ as the angular range for beam steering has been made due to the fact that for the physical aperture size considered here ($\approx 6.33\lambda_0 \times 6.33\lambda_0$), division into 8 sub-apertures along each transverse spatial dimension yields very limited aperture size for each sub-array making the beam steering toward end-fire angles inefficient in the account of further decrement in the effective aperture size as the beam steering angle grows steeper. This limitation can be circumvented by enlarging the metasurface aperture to increase the effective aperture size of the sub-arrays for steeper anomalous reflection angles.

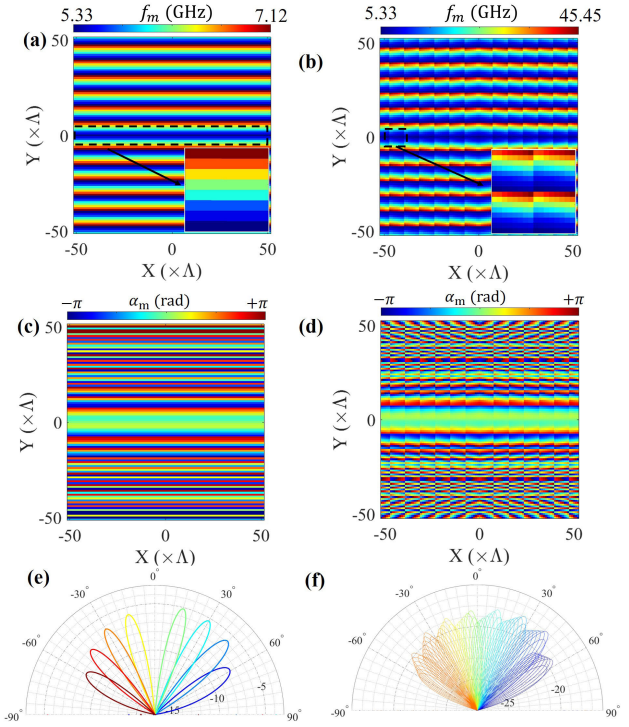

FIGURE 8. The spatial distribution of modulation frequency across (a) the 1D-interleaved and (b) 2D-interleaved STSAMs. The spatial distribution of modulation phase delay across (c) the 1D-interleaved and (d) 2D-interleaved STSAMs in order to generate 8 and 64 independent frequency channels,respectively at the first-order frequency harmonics of the sub-arrays pointing toward equally-spaced elevation angles in the range of $-60° < \theta < 60°$ in the elevation plane ($|\varphi| = 90°$). The farfield plots of the STSAM gain corresponding to (e) the 1D-interleaved and (f) 2D-interleaved STSAMs at the first-order frequency harmonics generated by the sub-arrays. The assigned color to each beam in (e) and (f) represents the modulation frequency of its corresponding sub-array.The assigned color to each beam represents the modulation frequency of its corresponding sub-array. For instance, in (e) the blue color beam corresponds to the modulation frequency of 5.33 GHz while the red one indicates 7.12 GHz.

The farfield patterns of STSAM antenna gain in all the established communication channels by the sub-arrays are shown in the elevation plane in Fig. 8(e) and (f) for the 1D-interleaved and 2D-interleaved STSAMs, respectively. It is clear that a directive beam is generated in each channel pointing toward the predefined direction with no apparent sidelobe. These results point toward the simultaneous and independent beam steering of such high-capacity STSAMs across multiple orthogonal frequency channels. The peak gains attained at the main lobe of the generated beams are considerably lower compared to the previous studied cases due to sharing of the

incident power between more channels. The peaks gains in the channels established by the 2D-interleaved STSAM are lower compared to those of its 1D-interleaved counterpart for the same reason.

As the final remark, it should be highlighted that all the established communication links by the 1D-interleaved and 2D-interleaved STSAM antennas are nonreciprocal in the account of broken time-reversal symmetry by the introduced time-modulation [59]. In particular, in the communication channel established by the p-th sub-array, a normally incident wave at the frequency of f_0 will undergo up-conversion of frequency ($f_0 \rightarrow f_0 + f_{m,p}$) while being anomalously reflected toward a specific direction which is determined by the progressive modulation phase delay of the unit cells forming the p-th sub-array. Now under time-reversal, the wave coming back in this channel from the same direction at the frequency of $f_0 + f_{m,p}$ will undergo up-conversion of frequency once again ($f_0 + f_{m,p} \rightarrow f_0 + 2f_{m,p}$) while being routed toward a direction which can be different from the broadside direction. As such, space-time gradient sub-arrays can isolate the forward and time-reversed light pathways in both space and time. Although the spatial isolation of up- and down-links in the nonreciprocal communication channels established by the STSAM is negligibly small when $f_{m,p} \ll f_0$ [51], the temporal isolation through frequency conversion operations rejects the interference between the signals in up- and down-links, thus enabling full-duplex communication (i.e. simultaneous transmission and reception) [94].

VII. CONCLUSION

In conclusion, we have introduced the concept of space-time shared aperture metasurfaces (STSAM) consisting of orthogonally modulated sub-array antennas interleaved within the same physical area. STSAMs are shown to enable adaptive multichannel communication through simultaneous and independent multifrequency multibeam scanning. Unlike quasi-static tunable metasurfaces relying on resonant phase modulation, the STSAMs exploit the dispersionless modulation-induced phase shift of higher-order frequency harmonics by tuning the modulation phase delay which not only enables attaining wide bandwidth, full angle-of-view, and ultralow SLL in dynamic beam steering but also allows for independent performance of interleaved sub-arrays with minimal cross-talk by avoiding nontrivial resonant coupling effects, thus dramatically enhancing the communication capacity through integration of several distinct channels into a single platform. We have theoretically realized STSAMs in the low-THz frequency regime by utilizing graphene patch micro-antennas as constituent unit cells whose surface conductivity can be modulated individually by applying RF biasing signals of different frequencies and phase delays via employing a 2D biasing networks. The modulation waveform of the metasurface is optimized to yield pure frequency mixing while minimizing the undesired frequency mixing products. The orthogonality condition of the established frequency channels by the sub-arrays is investigated and the condition for avoiding the cross-talk between them is identified. The simultaneous and independent real-time beam steering performance of the STSAM with full angle-of-view over the orthogonal frequency channels is demonstrated and the effect of array architecture on redistribution of the power between the channels is investigated. We have considered both 1D-interleaved and 2D-interleaved STSAMs for multibeam scanning along elevation and azimuth angles and established an upper bound on the capacity and number of orthogonal channels that can be obtained via 1D and 2D-interleaved STSAMs without compromising the angle-of-view. We have demonstrated that eight distinct channels can be obtained in 1D interleaved STSAM while for the two-dimensional scenario the number of independent channels can be further increased to 64.

Although our studies have been limited to a single incident frequency, considering the dispersionless property of the modulation-induced phase gradient, a similar performance can be obtained for different incident frequencies albeit with different efficiencies depending on the dispersive response of the metasurface. As such, our results point toward an approach for implementation of high-capacity multiple-input, MIMO smart array antennas for future generations of high-speed THz communication networks. The proposed concept of shared aperture in space-time not only is a promising approach toward enabling multichannel communication via multifrequency multibeam scanning but also can be applied for multiplexing any arbitrary beam-shaping functionalities.

REFERENCES

[1] I. F. Akyildiz, J. M. Jornet, and C. Han, "Terahertz band: Next frontier for wireless communications," *Phys. Commun.*, vol. 12, pp. 16–32, Sep. 2014.
[2] Z. Chen, X. Ma, B. Zhang, Y. X. Zhang, Z. Niu, N. Kuang, W. Chen, L. Li, and S. Li, "A survey on terahertz communications," *China Commun.*, vol. 16, no. 2, pp. 1–35, Feb. 2019.
[3] D. Bandyopadhyay and J. Sen, "Internet of Things: Applications and challenges in technology and standardization," *Wireless Pers. Commun.*, vol. 58, no. 1, pp. 49–69, May 2011.
[4] I. F. Akyildiz and J. M. Jornet, "The Internet of nano-things," *IEEE Wireless Commun.*, vol. 17, no. 6, pp. 58–63, Dec. 2010.
[5] Y. J. Cheng, X. Y. Bao, and Y. X. Guo, "60-GHz LTCC miniaturized substrate integrated multibeam array antenna with multiple polarizations," *IEEE Trans. Antennas Propag.*, vol. 61, no. 12, pp. 5958–5967, Dec. 2013.
[6] L. G. Sodin, "Method of synthesizing a beam-forming device for the N-beam and N-element array antenna, for any n," *IEEE Trans. Antennas Propag.*, vol. 60, no. 4, pp. 1771–1776, Apr. 2012.
[7] J. M. Montero, A. M. Ocampo, and N. J. G. Fonseca, "C-band multiple beam antennas for communication satellites," *IEEE Trans. Antennas Propag.*, vol. 63, no. 4, pp. 1263–1275, Apr. 2015.
[8] H. Barati, M. H. Fakheri, and A. Abdolali, "Experimental demonstration of metamaterial-assisted antenna beam deflection through folded transformation optics," *J. Opt.*, vol. 20, no. 8, Aug. 2018, Art. no. 085101.
[9] H. B. Sedeh, M. H. Fakheri, and A. Abdolali, "Advanced synthesis of meta-antenna radiation pattern enabled by transformation optics," *J. Opt.*, vol. 21, no. 4, Apr. 2019, Art. no. 045108.
[10] H. Barati, M. H. Fakheri, and A. Abdolali, "Exploiting transformation optics for arbitrary manipulation of antenna radiation pattern," *IET Microw., Antennas Propag.*, vol. 13, no. 9, pp. 1271–1279, Jul. 2019.
[11] J. Yang, M. Huang, J. Peng, and Z. Xiao, "Design of multi-beam antennas based on Epsilon-Near-Zero metamaterials," *AEU-Int. J. Electron. Commun.*, vol. 65, no. 6, pp. 543–547, Jun. 2011.
[12] Q. Cheng, W. Xiang Jiang, and T. Jun Cui, "Multi-beam generations at pre-designed directions based on anisotropic zero-index metamaterials," *Appl. Phys. Lett.*, vol. 99, no. 13, Sep. 2011, Art. no. 131913.

[13] H. F. Ma, X. Chen, X. M. Yang, W. X. Jiang, and T. J. Cui, "Design of multibeam scanning antennas with high gains and low sidelobes using gradient-index metamaterials," *J. Appl. Phys.*, vol. 107, no. 1, Jan. 2010, Art. no. 014902.

[14] S. M. A. M. H. Abadi and N. Behdad, "Design of wideband, FSS-based MultiBeam antennas using the effective medium approach," *IEEE Trans. Antennas Propag.*, vol. 62, no. 11, pp. 5557–5564, Nov. 2014.

[15] Y. Song Zhang and W. Hong, "A millimeter-wave gain enhanced multi-beam antenna based on a coplanar cylindrical dielectric lens," *IEEE Trans. Antennas Propag.*, vol. 60, no. 7, pp. 3485–3488, Jul. 2012.

[16] M. Huang, S. Yang, F. Gao, R. Quarfoth, and D. Sievenpiper, "A 2-D multibeam half maxwell fish-eye lens antenna using high impedance surfaces," *IEEE Antennas Wireless Propag. Lett.*, vol. 13, pp. 365–368, 2014.

[17] M. Farmahini-Farahani and H. Mosallaei, "Birefringent reflectarray metasurface for beam engineering in infrared," *Opt. Lett.*, vol. 38, no. 4, pp. 462–464, 2013.

[18] Y. B. Li, X. Wan, B. G. Cai, Q. Cheng, and T. J. Cui, "Frequency-controls of electromagnetic multi-beam scanning by metasurfaces," *Sci. Rep.*, vol. 4, no. 1, p. 6921, May 2015.

[19] H. F. Ma, Y. Q. Liu, K. Luan, and T. J. Cui, "Multi-beam reflections with flexible control of polarizations by using anisotropic metasurfaces," *Sci. Rep.*, vol. 6, no. 1, p. 39390, Dec. 2016.

[20] L. Bao, R. Y. Wu, X. Fu, Q. Ma, G. D. Bai, J. Mu, R. Jiang, and T. J. Cui, "Multi-beam forming and controls by metasurface with phase and amplitude modulations," *IEEE Trans. Antennas Propag.*, vol. 67, no. 10, pp. 6680–6685, Oct. 2019.

[21] J. Cheng, S. Inampudi, and H. Mosallaei, "Optimization-based dielectric metasurfaces for angle-selective multifunctional beam deflection," *Sci. Rep.*, vol. 7, no. 1, pp. 1–10, Dec. 2017.

[22] A. Forouzmand and H. Mosallaei, "Shared aperture antenna for simultaneous two-dimensional beam steering at near-infrared and visible," *J. Nanophotonics*, vol. 11, no. 1, Feb. 2017, Art. no. 010501.

[23] D. Gonzalez-Ovejero, G. Minatti, G. Chattopadhyay, and S. Maci, "Multi-beam by metasurface antennas," *IEEE Trans. Antennas Propag.*, vol. 65, no. 6, pp. 2923–2930, Jun. 2017.

[24] S. J. Li, Y. B. Li, H. Li, Z. X. Wang, C. Zhang, Z. X. Guo, R. Q. Li, X. Y. Cao, Q. Cheng, and T. J. Cui, "A thin self-feeding janus metasurface for manipulating incident waves and emitting radiation waves simultaneously," *Annalen der Physik*, vol. 532, no. 5, May 2020, Art. no. 2000020.

[25] S. J. Li, T. J. Cui, Y. B. Li, C. Zhang, R. Q. Li, X. Y. Cao, and Z. X. Guo, "Multifunctional and multiband fractal metasurface based on inter-metamolecular coupling interaction," *Adv. Theory Simul.*, vol. 2, no. 8, 2019, Art. no. 1900105.

[26] N. Yu and F. Capasso, "Flat optics with designer metasurfaces," *Nature Mater.*, vol. 13, no. 2, pp. 139–150, Feb. 2014.

[27] F. Ding, A. Pors, and S. I. Bozhevolnyi, "Gradient metasurfaces: A review of fundamentals and applications," *Rep. Prog. Phys.*, vol. 81, no. 2, Feb. 2018, Art. no. 026401.

[28] L. L. Shafai, W. A. Chamma, M. Barakat, P. C. Strickland, and G. Seguin, "Dual-band dual-polarized perforated microstrip antennas for SAR applications," *IEEE Trans. Antennas Propag.*, vol. 48, no. 1, pp. 58–66, 2000.

[29] R. L. Haupt, "Interleaved thinned linear arrays," *IEEE Trans. Antennas Propag.*, vol. 53, no. 9, pp. 2858–2864, Sep. 2005.

[30] C. I. Coman, I. E. Lager, and L. P. Ligthart, "The design of shared aperture antennas consisting of differently sized elements," *IEEE Trans. Antennas Propag.*, vol. 54, no. 2, pp. 376–383, Feb. 2006.

[31] C.-X. Mao, S. Gao, Q. Luo, T. Rommel, and Q.-X. Chu, "Low-cost X/Ku/Ka-band dual-polarized array with shared aperture," *IEEE Trans. Antennas Propag.*, vol. 65, no. 7, pp. 3520–3527, Jul. 2017.

[32] E. Maguid, I. Yulevich, D. Veksler, V. Kleiner, M. L. Brongersma, and E. Hasman, "Photonic spin-controlled multifunctional shared-aperture antenna array," *Science*, vol. 352, no. 6290, pp. 1202–1206, Jun. 2016.

[33] D. Lin, A. L. Holsteen, E. Maguid, G. Wetzstein, P. G. Kik, E. Hasman, and M. L. Brongersma, "Photonic multitasking interleaved Si nanoantenna phased array," *Nano Lett.*, vol. 16, no. 12, pp. 7671–7676, Dec. 2016.

[34] E. Maguid, I. Yulevich, M. Yannai, V. Kleiner, M. L. Brongersma, and E. Hasman, "Multifunctional interleaved geometric-phase dielectric metasurfaces," *Light, Sci. Appl.*, vol. 6, no. 8, p. e17027, Aug. 2017.

[35] A. Forouzmand and H. Mosallaei, "Composite multilayer shared-aperture nanostructures: A functional multispectral control," *ACS Photon.*, vol. 5, no. 4, pp. 1427–1439, Apr. 2018.

[36] G. D. Bai, Q. Ma, S. Iqbal, L. Bao, H. B. Jing, L. Zhang, H. T. Wu, R. Y. Wu, H. C. Zhang, C. Yang, and T. J. Cui, "Multitasking shared aperture enabled with multiband digital coding metasurface," *Adv. Opt. Mater.*, vol. 6, no. 21, Nov. 2018, Art. no. 1800657.

[37] L. Kang, R. P. Jenkins, and D. H. Werner, "Recent progress in active optical metasurfaces," *Adv. Opt. Mater.*, vol. 7, no. 14, Jul. 2019, Art. no. 1801813.

[38] T. Cui, B. Bai, and H. Sun, "Tunable metasurfaces based on active materials," *Adv. Funct. Mater.*, vol. 29, no. 10, Mar. 2019, Art. no. 1806692.

[39] Q. He, S. Sun, and L. Zhou, "Tunable/reconfigurable metasurfaces: Physics and applications," *Res.*, vol. 2019, Jul. 2019., Art. no. 1849272.

[40] A. M. Shaltout, V. M. Shalaev, and M. L. Brongersma, "Spatiotemporal light control with active metasurfaces," *Science*, vol. 364, no. 6441, May 2019, Art. no. eaat3100.

[41] Y.-W. Huang, H. W. H. Lee, R. Sokhoyan, R. A. Pala, K. Thyagarajan, S. Han, D. P. Tsai, and H. A. Atwater, "Gate-tunable conducting oxide metasurfaces," *Nano Lett.*, vol. 16, pp. 5319–5325, Aug. 2016.

[42] J. Park, J.-H. Kang, S. J. Kim, X. Liu, and M. L. Brongersma, "Dynamic reflection phase and polarization control in metasurfaces," *Nano Lett.*, vol. 17, no. 1, pp. 407–413, Jan. 2017.

[43] G. K. Shirmanesh, R. Sokhoyan, P. C. Wu, and H. A. Atwater, "Electro-optically tunable multifunctional metasurfaces," *ACS Nano*, vol. 14, no. 6, pp. 6912–6920, Jun. 2020.

[44] Z. Miao, Q. Wu, X. Li, Q. He, K. Ding, Z. An, Y. Zhang, and L. Zhou, "Widely tunable terahertz phase modulation with gate-controlled graphene metasurfaces," *Phys. Rev. X*, vol. 5, no. 4, Nov. 2015, Art. no. 041027.

[45] M. C. Sherrott, P. W. Hon, K. T. Fountaine, J. C. Garcia, S. M. Ponti, V. W. Brar, L. A. Sweatlock, and H. A. Atwater, "Experimental demonstration of >230 phase modulation in gate-tunable graphene–gold reconfigurable mid-infrared metasurfaces," *Nano Lett.*, vol. 17, no. 5, pp. 3027–3034, 2017.

[46] O. Balci, N. Kakenov, E. Karademir, S. Balci, S. Cakmakyapan, E. O. Polat, H. Caglayan, E. Özbay, and C. Kocabas, "Electrically switchable metadevices via graphene," *Sci. Adv.*, vol. 4, no. 1, Jan. 2018, Art. no. eaao1749.

[47] R. Sabri, A. Forouzmand, and H. Mosallaei, "Multi-wavelength voltage-coded metasurface based on indium tin oxide: Independently and dynamically controllable near-infrared multi-channels," *Opt. Express*, vol. 28, no. 3, pp. 3464–3481, 2020.

[48] S. Taravati and A. A. Kishk, "Space-time modulation: Principles and applications," *IEEE Microw. Mag.*, vol. 21, no. 4, pp. 30–56, Apr. 2020.

[49] C. Caloz and Z.-L. Deck-Leger, "Spacetime Metamaterials—Part I: General concepts," *IEEE Trans. Antennas Propag.*, vol. 68, no. 3, pp. 1569–1582, Mar. 2020.

[50] C. Caloz and Z.-L. Deck-Leger, "Spacetime Metamaterials—Part II: Theory and applications," *IEEE Trans. Antennas Propag.*, vol. 68, no. 3, pp. 1583–1598, Mar. 2020.

[51] A. Shaltout, A. Kildishev, and V. Shalaev, "Time-varying metasurfaces and Lorentz non-reciprocity," *Opt. Mater. Exp.*, vol. 5, no. 11, pp. 2459–2467, 2015.

[52] Y. Hadad, D. L. Sounas, and A. Alu, "Space-time gradient metasurfaces," *Phys. Rev. B, Condens. Matter*, vol. 92, no. 10, Sep. 2015, Art. no. 100304.

[53] Y. Shi and S. Fan, "Dynamic non-reciprocal meta-surfaces with arbitrary phase reconfigurability based on photonic transition in meta-atoms," *Appl. Phys. Lett.*, vol. 108, no. 2, Jan. 2016, Art. no. 021110.

[54] Y. Shi, S. Han, and S. Fan, "Optical circulation and isolation based on indirect photonic transitions of guided resonance modes," *ACS Photon.*, vol. 4, no. 7, pp. 1639–1645, Jul. 2017.

[55] L. Zhang, X. Q. Chen, R. W. Shao, J. Y. Dai, Q. Cheng, G. Castaldi, V. Galdi, and T. J. Cui, "Breaking reciprocity with space-time-coding digital metasurfaces," *Adv. Mater.*, vol. 31, no. 41, 2019, Art. no. 1904069.

[56] S. Taravati and G. V. Eleftheriades, "Full-duplex Nonreciprocal-Beam-Steering metasurfaces comprising time-modulated twin meta-atoms," 2019, *arXiv:1911.04033*. [Online]. Available: http://arxiv.org/abs/1911.04033

[57] J. W. Zang, D. Correas-Serrano, J. T. S. Do, X. Liu, A. Alvarez-Melcon, and J. S. Gomez-Diaz, "Nonreciprocal wavefront engineering with time-modulated gradient metasurfaces," *Phys. Rev. A, Gen. Phys.*, vol. 11, no. 5, May 2019, Art. no. 054054.

[58] X. Wang, A. Díaz-Rubio, H. Li, S. A. Tretyakov, and A. Alú, "Theory and design of multifunctional space-time metasurfaces," *Phys. Rev. A, Gen. Phys.*, vol. 13, no. 4, Apr. 2020, Art. no. 044040.

[59] D. L. Sounas and A. Alú, "Non-reciprocal photonics based on time modulation," *Nature Photon.*, vol. 11, no. 12, pp. 774–783, Dec. 2017.

[60] M. M. Salary, S. Jafar-Zanjani, and H. Mosallaei, "Electrically tunable harmonics in time-modulated metasurfaces for wavefront engineering," *New J. Phys.*, vol. 20, no. 12, Dec. 2018, Art. no. 123023.
[61] M. Liu, D. A. Powell, Y. Zarate, and I. V. Shadrivov, "Huygens' metadevices for parametric waves," *Phys. Rev. X*, vol. 8, no. 3, p. 031077, 2018.
[62] L. Zhang, X. Q. Chen, S. Liu, Q. Zhang, J. Zhao, J. Y. Dai, G. D. Bai, X. Wan, Q. Cheng, G. Castaldi, V. Galdi, and T. J. Cui, "Space-time-coding digital metasurfaces," *Nat. Commun.*, vol. 9, pp. 1–11, Oct. 2018.
[63] M. Mahdi Salary and H. Mosallaei, "Time-modulated conducting oxide metasurfaces for adaptive multiple access optical communication," *IEEE Trans. Antennas Propag.*, vol. 68, no. 3, pp. 1628–1642, Mar. 2020.
[64] H. Barati Sedeh, M. M. Salary, and H. Mosallaei, "Topological space-time photonic transitions in angular-momentum-biased metasurfaces," *Adv. Opt. Mater.*, vol. 8, no. 11, 2020, Art. no. 2000075.
[65] S. Inampudi, M. M. Salary, S. Jafar-Zanjani, and H. Mosallaei, "Rigorous space-time coupled-wave analysis for patterned surfaces with temporal permittivity modulation," *Opt. Mater. Express*, vol. 9, no. 1, pp. 162–182, 2019.
[66] M. M. Salary, S. Farazi, and H. Mosallaei, "A dynamically modulated all-dielectric metasurface doublet for directional harmonic generation and manipulation in transmission," *Adv. Opt. Mater.*, vol. 7, no. 23, 2019, Art. no. 1900843.
[67] H. Barati Sedeh, M. M. Salary, and H. Mosallaei, "Time-varying optical vortices enabled by time-modulated metasurfaces," *Nanophotonics*, vol. 9, no. 9, pp. 2957–2976, Jul. 2020.
[68] E. Galiffi, P. A. Huidobro, and J. B. Pendry, "Broadband nonreciprocal amplification in luminal metamaterials," *Phys. Rev. Lett.*, vol. 123, no. 20, Nov. 2019, Art. no. 206101.
[69] S. Taravati and G. V. Eleftheriades, "Space-time medium functions as a perfect Antenna-Mixer-Amplifier transceiver," 2020, *arXiv:2005.00807*. [Online]. Available: http://arxiv.org/abs/2005.00807
[70] M. S. Mirmoosa, G. A. Ptitcyn, V. S. Asadchy, and S. A. Tretyakov, "Time-varying reactive elements for extreme accumulation of electromagnetic energy," *Phys. Rev. A, Gen. Phys.*, vol. 11, no. 1, Jan. 2019, Art. no. 014024.
[71] A. Shlivinski and Y. Hadad, "Beyond the bode-fano bound: Wideband impedance matching for short pulses using temporal switching of transmission-line parameters," *Phys. Rev. Lett.*, vol. 121, no. 20, Nov. 2018, Art. no. 204301.
[72] Y. Sivan and J. B. Pendry, "Time reversal in dynamically tuned zero-gap periodic systems," *Phys. Rev. Lett.*, vol. 106, no. 19, May 2011, Art. no. 193902.
[73] N. Chamanara and C. Caloz, "Linear pulse compansion using co-propagating space-time modulation," 2018, *arXiv:1810.04129*. [Online]. Available: http://arxiv.org/abs/1810.04129
[74] N. Chamanara, Y. Vahabzadeh, and C. Caloz, "Simultaneous control of the spatial and temporal spectra of light with space-time varying metasurfaces," *IEEE Trans. Antennas Propag.*, vol. 67, no. 4, pp. 2430–2441, Apr. 2019.
[75] M. Liu, A. B. Kozyrev, and I. V. Shadrivov, "Time-varying metasurfaces for broadband spectral camouflage," *Phys. Rev. A, Gen. Phys.*, vol. 12, no. 5, Nov. 2019, Art. no. 054052.
[76] X. Wang and C. Caloz, "Spread-spectrum selective camouflaging based on time-modulated metasurface," 2019, *arXiv:1909.04480*. [Online]. Available: http://arxiv.org/abs/1909.04480
[77] M. Jablan, H. Buljan, and M. Soljačić, "Plasmonics in graphene at infrared frequencies," *Phys. Rev. B*, vol. 80, no. 24, Dec. 2009, Art. no. 245435.
[78] L. Ju, B. Geng, J. Horng, C. Girit, M. Martin, Z. Hao, H. A. Bechtel, X. Liang, A. Zettl, Y. R. Shen, and F. Wang, "Graphene plasmonics for tunable terahertz metamaterials," *Nature Nanotechnol.*, vol. 6, no. 10, pp. 630–634, Sep. 2011.
[79] C. T. Phare, Y.-H. Daniel Lee, J. Cardenas, and M. Lipson, "Graphene electro-optic modulator with 30 GHz bandwidth," *Nature Photon.*, vol. 9, no. 8, pp. 511–514, Aug. 2015.
[80] Q. Ma, Q. R. Hong, X. X. Gao, H. B. Jing, C. Liu, G. D. Bai, Q. Cheng, and T. J. Cui, "Smart sensing metasurface with self-defined functions in dual polarizations," *Nanophotonics*, vol. 9, no. 10, pp. 3271–3278, Apr. 2020.
[81] X. G. Zhang, Q. Yu, W. X. Jiang, Y. L. Sun, L. Bai, Q. Wang, C. Qiu, and T. J. Cui, "Polarization-controlled dual-programmable metasurfaces," *Adv. Sci.*, vol. 7, no. 11, Jun. 2020, Art. no. 1903382.
[82] E. Carrasco, M. Tamagnone, and J. Perruisseau-Carrier, "Tunable graphene reflective cells for THz reflectarrays and generalized law of reflection," *Appl. Phys. Lett.*, vol. 102, no. 10, Mar. 2013, Art. no. 104103.
[83] K. Rouhi, H. Rajabalipanah, and A. Abdolali, "Multi-bit graphene-based bias-encoded metasurfaces for real-time terahertz wavefront shaping: From controllable orbital angular momentum generation toward arbitrary beam tailoring," *Carbon*, vol. 149, pp. 125–138, Aug. 2019.
[84] G. W. Hanson, "Dyadic Green's functions for an anisotropic, non-local model of biased graphene," *IEEE Trans. Antennas Propag.*, vol. 56, no. 3, pp. 747–757, Mar. 2008.
[85] S. Rakheja and P. Sengupta, "Gate-voltage tunability of plasmons in single-layer graphene structures—Analytical description, impact of interface states, and concepts for terahertz devices," *IEEE Trans. Nanotechnol.*, vol. 15, no. 1, pp. 113–121, Jan. 2016.
[86] A. S. Mayorov, R. V. Gorbachev, S. V. Morozov, L. Britnell, R. Jalil, L. A. Ponomarenko, P. Blake, K. S. Novoselov, K. Watanabe, T. Taniguchi, and A. K. Geim, "Micrometer-scale ballistic transport in encapsulated graphene at room temperature," *Nano Lett.*, vol. 11, no. 6, pp. 2396–2399, Jun. 2011.
[87] C. Hwang, D. A. Siegel, S.-K. Mo, W. Regan, A. Ismach, Y. Zhang, A. Zettl, and A. Lanzara, "Fermi velocity engineering in graphene by substrate modification," *Sci. Rep.*, vol. 2, no. 1, p. 590, Dec. 2012.
[88] L. Banszerus, M. Schmitz, S. Engels, J. Dauber, M. Oellers, F. Haupt, K. Watanabe, T. Taniguchi, B. Beschoten, and C. Stampfer, "Ultrahigh-mobility graphene devices from chemical vapor deposition on reusable copper," *Sci. Adv.*, vol. 1, no. 6, Jul. 2015, Art. no. e1500222.
[89] L. Banszerus, T. Sohier, A. Epping, F. Winkler, F. Libisch, F. Haupt, K. Watanabe, T. Taniguchi, K. Müller-Caspary, N. Marzari, F. Mauri, B. Beschoten, and C. Stampfer, "Extraordinary high room-temperature carrier mobility in graphene-WSeExtraordinary high room-temperature carrier mobility in graphene-WSe_2 heterostructures 2 heterostructures," 2019, *arXiv:1909.09523*. [Online]. Available: http://arxiv.org/abs/1909.09523
[90] G. Kafaie Shirmanesh, R. Sokhoyan, R. A. Pala, and H. A. Atwater, "Dual-gated active metasurface at 1550 nm with wide (> 300°) phase tunability," *Nano Lett.*, vol. 18, no. 5, pp. 2957–2963, 2018.
[91] M. G. Moharam, E. B. Grann, D. A. Pommet, and T. K. Gaylord, "Formulation for stable and efficient implementation of the rigorous coupled-wave analysis of binary gratings," *J. Opt. Soc. Amer. A, Opt. Image Sci.*, vol. 12, no. 5, pp. 1068–1076, 1995.
[92] S. Inampudi, V. Toutam, and S. Tadigadapa, "Robust visibility of graphene monolayer on patterned plasmonic substrates," *Nanotechnology*, vol. 30, no. 1, Jan. 2019, Art. no. 015202.
[93] C. A. Balanis, *Antenna Theory: Analysis and Design*. Hoboken, NJ, USA: Wiley, 2016.
[94] M. M. Salary, S. Jafar-Zanjani, and H. Mosallaei, "Nonreciprocal optical links based on time-modulated nanoantenna arrays: Full-duplex communication," *Phys. Rev. B, Condens. Matter*, vol. 99, no. 4, Jan. 2019, Art. no. 045416.

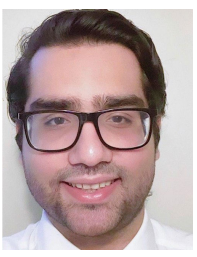

HOOMAN BARATI SEDEH (Student Member, IEEE) received the B.Sc. degree in electrical engineering-communications from the Iran University of Science and Technology, Tehran, Iran, in 2019. He is currently pursuing the M.Sc. degree in electrical engineering-electromagnetics with Northeastern University, Boston, MA, USA. His current research interests include studying the effects of introducing temporal variation in physical systems and design of optical metasurfaces.

MOHAMMAD MAHDI SALARY received the M.Sc. and Ph.D. degrees in electrical engineering from Northeastern University, Boston, MA, USA, in 2017 and 2020, respectively. His current research interests include modeling and design of photonic metamaterials with a major focus on multiscale and multiphysics phenomena. He was a recipient of Honorable Mention Student Paper Award from the IEEE International Symposium on Antennas and Propagation in 2019.

HOSSEIN MOSALLAEI (Senior Member, IEEE) received the Ph.D. degree in electrical engineering from the University of California, Los Angeles (UCLA), 2001. From 2002 to 2005, he was a Research Scientist with the Department of EECS, University of Michigan. He is currently a Full Professor of electrical and computer engineering with the College of Engineering, Northeastern University. He is also the Director of Metamaterials Laboratory, Northeastern University, with research focus on theory and design computation of active and tunable metamaterials and metasurfaces. He is the holder of two U.S. patents. He has authored and coauthored over 200 technical journal articles and conference papers. He is also a Full Member of URSI and a member of American Association for the Advancement of Science. He is listed in Whos Who in Science and Engineering, in America, and in the World. He was a recipient of student prize paper awards in AP-S 2000, 2001, 2003, and 2005 along with his students, URSI Young Scientist Award in 2001, and RMTG Award in 2002.